nature aging

Article

https://doi.org/10.1038/s43587-024-00691-3

Restoration of cervical lymphatic vessel function in aging rescues cerebrospinal fluid drainage

Received: 11 January 2023

Accepted: 16 July 2024

Published online: 15 August 2024

Check for updates

Ting Du[1,7], Aditya Raghunandan[2,3,7], Humberto Mestre[1,4,7], Virginia Plá[1,5], Guojun Liu[1], Antonio Ladrón-de-Guevara[1,6], Evan Newbold[1], Paul Tobin[1], Daniel Gahn-Martinez[1], Saurav Pattanayak[1], Qinwen Huang[1], Weiguo Peng[1], Maiken Nedergaard[1,5] ✉ & Douglas H. Kelley[2] ✉

Cervical lymphatic vessels (cLVs) have been shown to drain solutes and cerebrospinal fluid (CSF) from the brain. However, their hydrodynamical properties have never been evaluated in vivo. Here, we developed two-photon optical imaging with particle tracking in vivo of CSF tracers (2P-OPTIC) in superficial and deep cLVs of mice, characterizing their flow and showing that the major driver is intrinsic pumping by contraction of the lymphatic vessel wall. Moreover, contraction frequency and flow velocity were reduced in aged mice, which coincided with a reduction in smooth muscle actin expression. Slowed flow in aged mice was rescued using topical application of prostaglandin $F_{2\alpha}$, a prostanoid that increases smooth muscle contractility, which restored lymphatic function in aged mice and enhanced central nervous system clearance. We show that cLVs are important regulators of CSF drainage and that restoring their function is an effective therapy for improving clearance in aging.

Lymphatic vessels (LVs) return 4–5 l of fluid from interstitial spaces back into venous circulation daily[1,2]. Their failure leads to diseases such as lymphedema and contributes to cancer metastasis, autoimmune disorders (for example, inflammatory bowel disease), glaucoma, obesity and cardiovascular disease. Although the central nervous system (CNS) lacks LVs, a network of astrocyte-lined perivascular spaces (glymphatic system) facilitates transport to LVs in the surrounding meninges[3,4] and along exiting cranial and spinal nerves[5] to drain fluid and solute to venous circulation. cLVs in the rodent neck are responsible for draining ~50% of CSF from the brain and into cervical lymph nodes (cLNs)[6–8], and this drainage pathway plays a role in animal models of Alzheimer's disease[9,10], Parkinson's disease[11], stroke[12] and traumatic brain injury[13,14]. Transport of CNS antigens to the periphery via cLVs also influences multiple sclerosis[15] and modulates immune checkpoint inhibitors in CNS tumors[16] and amyloid-β immunotherapy[9] in rodents. cLVs also contribute to fluid homeostasis[17], suggesting that healthy cLVs are crucial for efficient fluid and solute clearance from the brain. However, the pumping and fluid transport properties of these vessels have not been directly assessed in vivo, and this is important since their function declines in aging[9,18–20] and coincides with increasing risk of age-related CNS diseases[7,21,22].

Collecting LVs in the abdomen and extremities drive flow via active (intrinsic) and passive (extrinsic) pumping. Active pumping is generated by rapid, phasic contractions of the smooth muscle cells (SMCs) lining the lymphangions, the functional units of LVs, which are separated by one-way valves that limit reflux and ensure unidirectional flow.

[1]Center for Translational Neuromedicine, Division of Glial Disease and Therapeutics, University of Rochester, Rochester, NY, USA. [2]Department of Mechanical Engineering, University of Rochester, Rochester, NY, USA. [3]Department of Mechanical Engineering, University of Michigan-Dearborn, Dearborn, MI, USA. [4]Department of Neurology, University of Pennsylvania, Philadelphia, PA, USA. [5]Center for Translational Neuromedicine, University of Copenhagen, Copenhagen, Denmark. [6]Department of Biomedical Engineering, University of Rochester, Rochester, NY, USA. [7]These authors contributed equally: Ting Du, Aditya Raghunandan, Humberto Mestre. ✉e-mail: nedergaard@urmc.rochester.edu; d.h.kelley@rochester.edu

https://doi.org/10.1038/s43587-024-00691-3

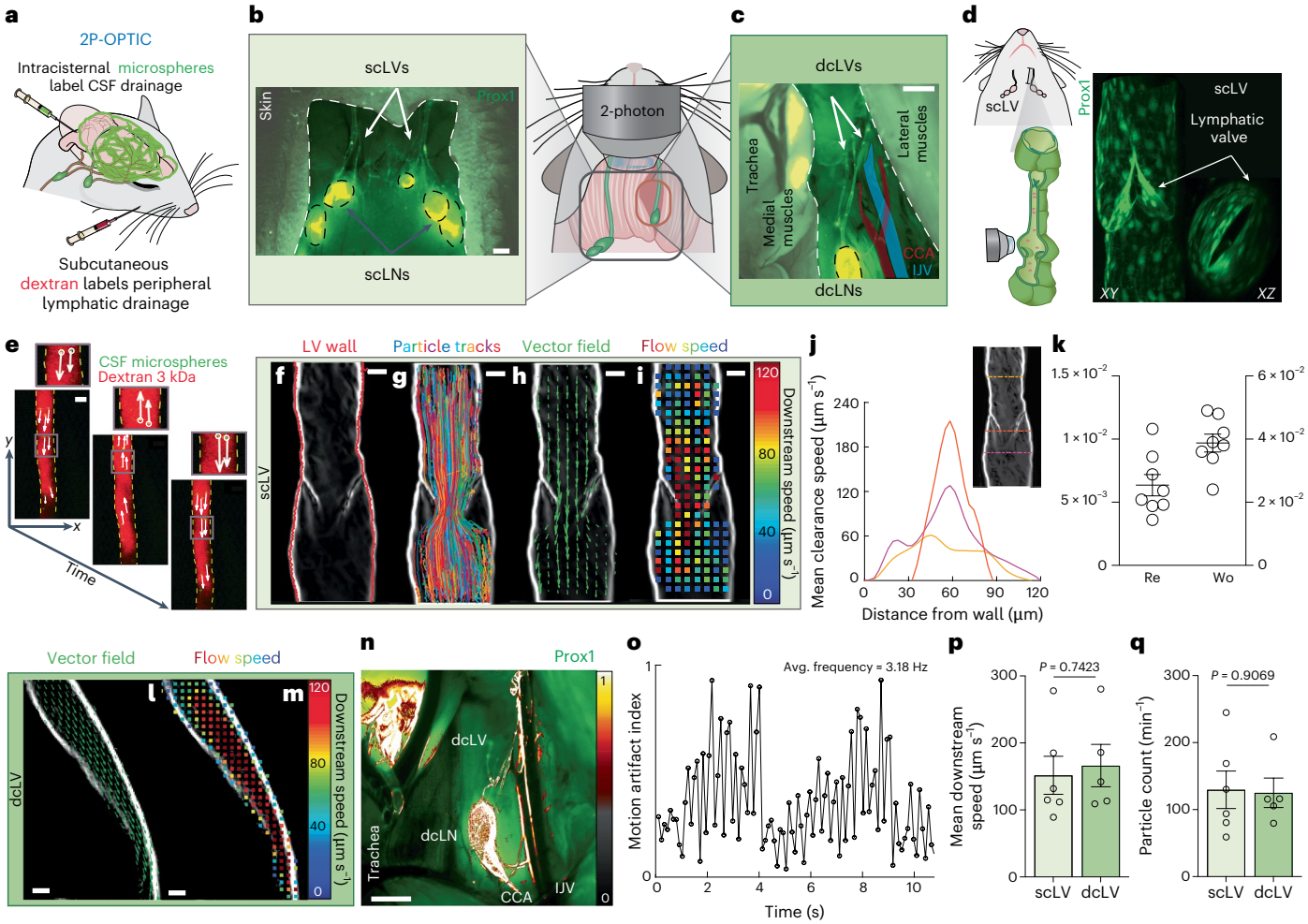

Fig. 1 | Two-photon optical imaging with particle tracking in vivo of CSF tracers (2P-OPTIC). a, 2P-OPTIC consists of an intracisternal injection of fluorescent microspheres to label CSF drainage and a subcutaneous cheek injection of a 3-kDa dextran to label peripheral lymphatic drainage. **b**,**c**, scLVs (**b**) and dcLVs (**c**) in anesthetized mice were surgically exposed. Scale bar, 1 mm. **d**, Two-photon microscopy was used to image cLVs (Prox1-GFP-positive) and valves. **e**, Particle tracking velocimetry was used to evaluate the flow in the LV and track the motion of the LV wall. The white arrows show the velocity of each microsphere, which tracks fluid motion (inset). Scale bar, 50 µm. **f**, The red outline represents the vessel wall, tracked to obtain changes to vessel diameter. **g**, Rainbow-colored lines represent superimposed trajectories of tracked fluorescent microspheres flowing in the scLV. **h**, The time-averaged velocity field (green arrows) quantifies net transport in the scLV. **i**, Boxes indicate the local time-averaged fluid speed of scLVs, which is slowest near vessel walls and fastest near the vessel center. **j**, Time-averaged velocity profiles measured upstream, downstream and at the valve indicate that highest centerline speeds are measured at the valve. Average flow speed profiles are plotted as a function of distance from the left wall of the scLV. Colored lines in the inset indicate the location of each profile of the scLV. Scale bar, 50 µm. **k**, Reynolds and Womersley numbers for the time-averaged flow of the scLV. Data are presented as the mean ± s.e.m.; $n = 8$ mice. **l**,**m**, The time-averaged velocity field (**l**) and local time-averaged downstream speed (**m**) show the net transport in a dcLV. Scale bar, 50 µm. **n**, Spatial motion artifact index, showing high artifact surrounding the trachea and LV/LN overlaying the common carotid artery (CCA) and the internal jugular vein (IJV). Scale bar, 1 mm. **o**, Average motion artifact index over time showing a ~3.18 Hz source of motion, suggestive of a cardiac origin. **p**,**q**, Mean downstream speed (**p**) and particle counts (**q**) for both scLVs and dcLVs. Two-sided unpaired *t*-test was performed. Data are presented as the mean ± s.e.m.; $n = 5$–6 mice per group.

Passive pumping relies on compression by contraction of the surrounding skeletal muscle. The respiratory and cardiac cycles may also propel lymph[23]. However, little is known about cLV pumping mechanisms, and existing techniques fail to provide spatially resolved flow rates and contractility dynamics in vivo[7,24–28].

To overcome these limitations, we developed two-photon optical imaging with particle tracking in vivo of CSF tracers (2P-OPTIC). This approach simultaneously measured flow speeds within a lymphangion, cLV contractility and solute transport, all in vivo and at high resolution. We show that in superficial cervical lymphatic vessels (scLVs), contractions are the primary flow driver, and these decline in aging, coinciding with a reduction in lymphatic smooth muscle actin (SMA) coverage. Furthermore, we demonstrate that the age-dependent decline of scLV function can be rescued by prostaglandin $F_{2\alpha}$ ($PGF_{2\alpha}$), a smooth muscle contractile agent[29,30]. We speculate that age-induced impairment of scLV function contributes to disease development[9,10], hinders injury recovery and blunts responses to immunotherapy, providing an opportunity for therapeutic intervention.

Results

Quantifying flow in cervical lymph vessels

scLVs and deep cervical lymphatic vessels (dcLVs) together drain fluid from the CNS and all remaining extracranial structures in the head and neck. To pinpoint transport of CNS-specific solutes, we used an approach termed 2P-OPTIC (Fig. 1a). To image cLVs and reduce photon scattering, both scLVs and dcLVs were surgically exposed. Superficial LVs lie just below the skin and can be seen through the superior cervical fascia, draining to superior cLNs (Fig. 1b). Because dcLVs sit medial to the common carotid artery and the internal jugular vein, visualization requires medial retraction of the trachea and medial musculature

https://doi.org/10.1038/s43587-024-00691-3

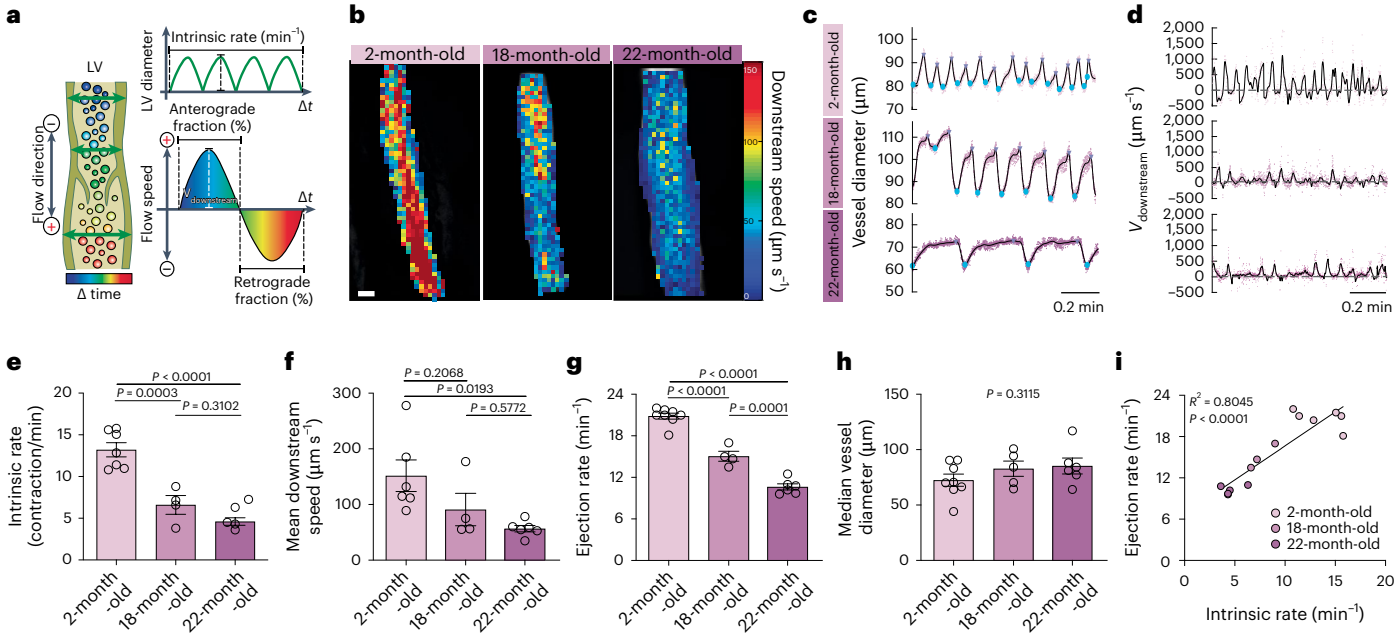

Fig. 2 | Intrinsic pump dysfunction in aging. a, Schematic of the various parameters computed to characterize LV pumping and flow properties. **b**, Representative images of the local time-averaged flow speed show that the lymph flow is nearly stagnant in aging. Scale bar, 50 μm **c**, Representative temporal variation of the median vessel diameter showed an age-dependent decrease in vessel function. Maxima and minima (diastolic and systolic peaks) are also indicated. **d**, Representative temporal variation of downstream velocity calculated from particle tracking for the different age groups showed the lymph flow speed decreased by aging. In **c** and **d**, the dots represent the raw data, and the solid lines were obtained by smoothing over a 500-ms window. **e**, Intrinsic rate (frequency of contraction). **f**,**g**, Mean downstream speed (**f**) and ejection rate (**g**) (frequency of curves shown in **c**) exhibited an age-dependent decrease. **h**, Median vessel diameter showed no change in aging. One-way analysis of variance (ANOVA) post hoc Tukey's test was performed (**e**–**h**). Data are presented as the mean ± s.e.m.; $n = 4$–7 mice per group. **i**, Linear regression of intrinsic rate and ejection rate with 95% confidence intervals for all aging groups indicates a strong correlation between contraction of cervical lymph vessel and lymph efflux.

(sternohyoid and omohyoid muscle) and lateral retraction of the lateral musculature (sternomastoid and posterior belly of the digastric muscle; Fig. 1c). LVs were labeled by intramuscular cheek injection of FITC–dextran (3 kDa). Two-photon resonant scanning microscopy was used to image each cLV in a single focal plane at 60 frames per second (Fig. 1d,e). The dextran labeled the draining lymph and enabled measurement of the vessel diameter (Fig. 1e). To parse out CNS-borne transport from extracranial drainage, we injected 1 μm fluorescent spheres into the cisterna magna[31]. We then used particle tracking velocimetry to quantify flow speeds in cLVs. Our methods allowed simultaneous measurements of contractility (Fig. 1f), flow speeds (Fig. 1g–i) and the cardiac and respiratory cycles (Extended Data Fig. 1 and Supplementary Videos 1 and 2). More than 1,000 particles were tracked during each 10-min experiment (Fig. 1g). Pre-nodal scLVs in 2-month-old mice were 72.4 ± 5.5 μm in diameter. Particle tracks were distributed nearly uniformly, with an increased concentration near valve centers. The time-averaged velocity showed net transport of lymph (Fig. 1h–i). Prior studies used fluorescence intensity of luminal dextran as a metric of LV transport[20], but in our data it was a poor predictor of LV flow speed and was primarily determined by LV diameter (Extended Data Fig. 2). In a typical contraction cycle, fluid flowed rapidly into the lymphangion while the downstream valve remained closed, and the vessel filled—in some cases inducing the vessel to expand further. With the downstream valve closed, there was then retrograde fluid motion that closed the upstream valve. Next, contraction of the lymphangion expelled fluid downstream to the next lymphangion (Supplementary Video 1). The time-averaged flow (Fig. 1i) showed an average velocity of 151.7 ± 28.4 μm s^{-1}, fastest near the vessel center and slowest near the walls (Fig. 1j), as expected for pressure-driven flows. In experiments where valves were visible, the highest speeds occurred at the valves (Fig. 1j), consistent with fluid accelerating through a smaller cross-section to maintain a constant flow rate. The Reynolds number, Re, is the ratio between the inertial and viscous forces, with Re > 1 indicating that inertia dominates and Re < 1 indicating that viscous forces dominate. In scLVs, we found Re = 0.0064 ± 0.0008 (Fig. 1k), implying that viscous forces dominate. The Womersley number, Wo, is the ratio of the viscous timescale to the pulsation time. In scLVs, we found Wo = 0.039 ± 0.003, suggesting that transient inertial effects are negligible (Fig. 1k). To our knowledge, lymphatic flow in scLVs in live rodents has not been described previously.

dcLVs had similar flow characteristics compared to scLVs (Fig. 1l,m); however, due to their proximity to the carotid artery and trachea, their visualization involved marked motion artifacts (Fig. 1n and Supplementary Video 2). The frequency of the artifacts was ~3.18 Hz, which coincides with the cardiac frequency, suggesting that cardiac pulsatility was the largest source of motion (Fig. 1o). Nonetheless, mean downstream flow speeds in dcLVs were comparable to those observed in scLVs (166.2 ± 31.6 μm s^{-1} versus 151.7 ± 28.4 μm s^{-1}; $P = 0.7423$; Fig. 1p), with all flows being laminar, viscosity-dominated flows (Re < 1). The total number of CNS-borne microspheres was also similar across the two LV chains (scLVs: 129.6 ± 28.0 particles per minute versus dcLVs: 125.2 ± 22.0 particles per minute; $P = 0.9069$; Fig. 1q), suggesting that both scLVs and dcLVs play a role in CSF drainage.

Lymphatic fluid drainage is impaired in aging

Efflux along cervical lymphatics declines in aged mice[7,18,20], but whether this is due to reduced function within the intracranial compartment or among cLVs has not been described. We evaluated the structure and function of scLVs using 2P-OPTIC in 2-month-old, 18-month-old and 22-month-old mice (Fig. 2 and Supplementary Video 3). Reynolds numbers in 18-month-old (0.0052 ± 0.0011) and 22-month-old (0.0041 ± 0.0008, $P = 0.2194$) mice and Womersley numbers (0.037 ± 0.003 and 0.033 ± 0.003 respectively, $P = 0.3440$) were comparable to those in young animals, indicating viscous flows and negligible inertial forces.

https://doi.org/10.1038/s43587-024-00691-3

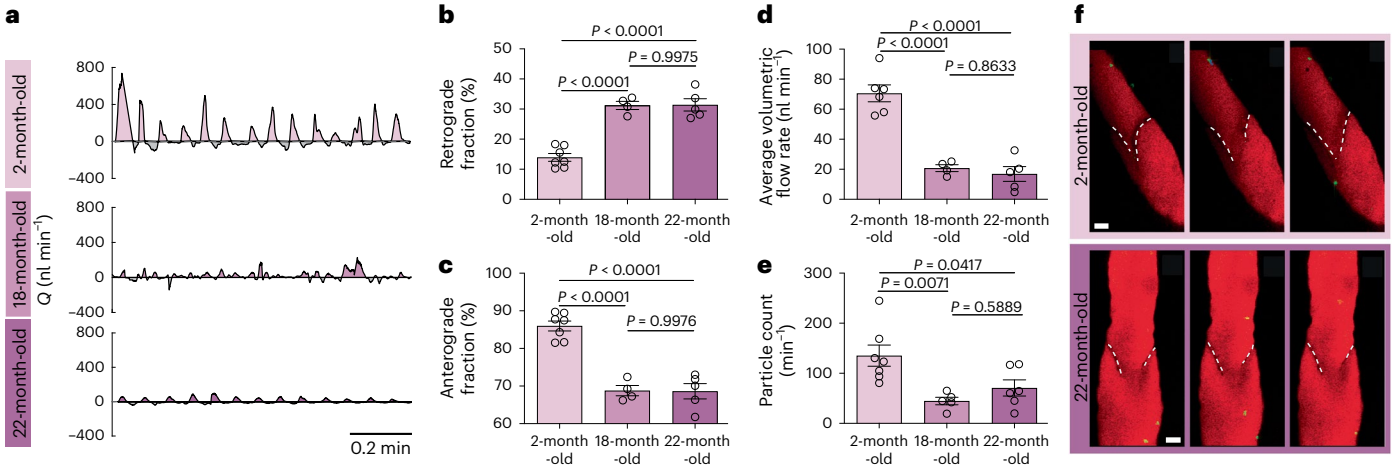

Fig. 3 | Lymphatic efflux volumes are reduced in old age. a, Temporal variation of the volume flow rate Q calculated from the product of the instantaneous spatially averaged downstream velocity and instantaneous cross-sectional lymphangion area. The lymphangion was assumed to have a circular cross-section, and the measured median vessel diameter was used to calculate the cross-sectional area. By definition, $Q > 0$ signifies anterograde flow, and $Q < 0$ signifies retrograde flow. **b**, The retrograde fraction was increased by aging. **c**–**e**, Anterograde fraction (**c**), average volume flow rate (**d**) and particle count (**e**) were all decreased by aging. One-way ANOVA post hoc Tukey's test was performed (**b**–**e**). Data are presented as the mean ± s.e.m. $n = 4$–7 mice per group. **f**, Representative images of valves (outlined by dashed lines) in young mice and old mice. Functional valves open and close to regulate flow in young mice but fail in old mice. Scale bar, 50 µm. $n = 4$–7 mice per group.

LV pumping and flow are characterized in Fig. 2a. Diameter was measured at 20 locations along the vessel for 10 min while flow was measured simultaneously (Fig. 2b,c). There were no differences in spatial median scLV diameter across ages, suggesting that scLVs reach adult size at 2 months of age (Fig. 2h). Despite similar sizes, average downstream velocity ($V_{downstream}$; Fig. 2d,f) declined by ~40% at 18 months (90.9 ± 29.1 µm s^{-1}, $P = 0.21$ versus 2 months) and was significantly slowed (~63%) at 22 months (56.6 ± 5.7 µm s^{-1}, $P = 0.02$ versus 2 months). scLVs expanded and contracted rapidly in young mice (13.2 ± 0.8 contractions per minute; Fig. 2e), with each cycle lasting around 4.6 s (Fig. 2c). This is consistent with previous studies that measured contraction dynamics in collecting LVs in the legs and flanks of young mice under a ketamine–xylazine anesthesia[32]. The intrinsic rate steeply declined in 18-month-old mice (50.0%, $P = 0.0003$) and further declined in 22-month-old mice (65%, $P < 0.0001$; Fig. 2e), suggesting an age-dependent slowing of the contractility of scLVs.

To evaluate lymphatic function, we quantified the ejection rate, defined as the pulsation frequency of the downstream velocity (Fig. 2d), for all age groups (Fig. 2g). The ejection rate may not match the intrinsic contraction rate but effectively represents the frequency of valves opening and closing, useful for evaluating valve function. We observed significant declines in the ejection rate from age 2 to 18 months (−27.8%, $P < 0.0001$) and from 18 to 22 months (−29.3%, $P = 0.0001$; Fig. 2g). These declines correlated with impairment of the intrinsic contraction rate (coefficient of determination (R^2) = 0.8045; Fig. 2i), implying that lymphangion contractility drives most of the flow. However, contrary to previous in vitro studies using isolated LVs, we did not observe a consistent one-to-one relationship between vessel contraction and flow oscillation[28,33]. This suggests that an in vivo lymphangion is influenced by upstream and downstream lymphangions, alluding to coordination among SMCs. Interestingly, lymphatic flow in scLVs was not dependent on heart or respiratory rate (Extended Data Fig. 1). These experiments show that aged cLVs have significantly lower contraction frequency, which results in reduced transport.

Lymphatic efflux volumes are reduced in aging

We defined the instantaneous volumetric flow rate (Q) as the product of the downstream velocity and the cross-sectional area (from the instantaneous spatial median diameter, assuming a circular cross-section; Fig. 3a). Maximum flow rate in young mice reached 724.2 nl min^{-1}, while flow rates drastically decreased in aged mice (18-month: 423.2 nl min^{-1}; and 22-month: 180.9 nl min^{-1}). Next, we computed the anterograde fraction, defined as the fraction of the time during which fluid flows away from the skull, and the retrograde fraction, defined as the fraction of time during which flow is retrograde (Fig. 3b–d). Not surprisingly, 2-month-old mice exhibited the highest anterograde fractions (85.9% ± 1.3%), indicating that lymphatic flow in young mice is primarily unidirectional, consistent with regulation by valves between lymphangions (Supplementary Video 4). Aged mice exhibited a lower anterograde fraction (68.8% ± 1.4% for 18-month-old, $P < 0.0001$ versus 2-month-old; 68.6% ± 2.0% for 22-month-old, $P < 0.0001$ versus 2-month-old; Fig. 3c). In aged mice, valves did not fully close (Fig. 3f and Supplementary Video 4), allowing particles to oscillate back and forth without being trapped in the imaged lymphangion (Supplementary Video 4). This suggests that aged valves are unable to limit reflux, resulting in the increased retrograde fractions. While dysfunctional valves have previously been implicated in reduced lymphatic transport in isolated aged mesenteric vessels[34], our observations document defects in valve function of scLVs in vivo and their role in reducing lymphatic drainage.

We quantified impairment according to the average volumetric flow rate, defined as the net volume of fluid transported downstream per minute (net area under the curves in Fig. 3a). In aged mice, less frequent contractions and lower anterograde fractions resulted in significantly lower volumes being ejected in 18-month-old (20.8 ± 2.3 nl min^{-1}, $P < 0.0001$) and 22-month-old (16.9 ± 4.9 nl min^{-1}, $P < 0.0001$) mice compared to 2-month-old mice (70.6 ± 5.6 nl min^{-1}; Fig. 3d). That is, an aged scLV transported lymph only about a quarter as fast (24.3 µl per day) as a young scLV (102 µl per day). We hypothesized that this flow reduction could also delay the arrival of CNS solutes (for example, signaling peptides, antigens and immune cells) to the cLNs. To test this idea, we counted the number of 1-µm particles passing through the field of view per minute as a measure of the transport rate of objects of similar size (Fig. 3e). Particle counts were significantly decreased in 18-month-old (44.5 ± 7.5) and 22-month-old (62.4 ± 16.1) mice compared to 2-month-old mice (104.8 ± 19.1, 63.9% and 49.4%, respectively; Fig. 3e), indicating that CNS-derived lymphatic efflux is severely compromised in aging.

Loss of SMA coverage in aging impairs LV contractility

Aged collecting LVs in other rodents display reduced contractility due to the loss of SMCs lining the lymphangions, decreased expression

https://doi.org/10.1038/s43587-024-00691-3

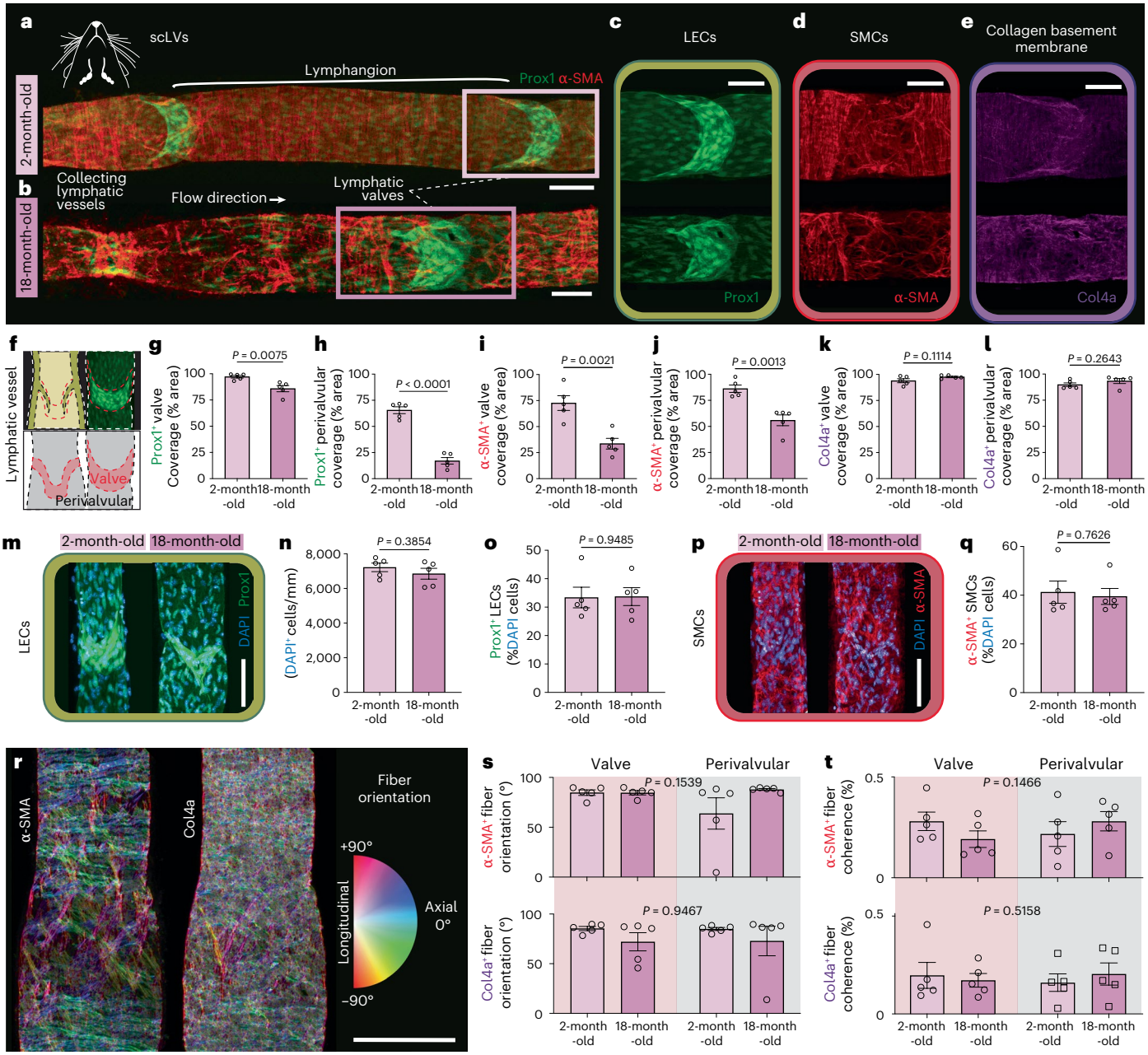

Fig. 4 | Aging causes loss of α-SMA coverage in scLVs. a,**b**, Representative images of collecting scLVs from (**a**) 2-month-old (**a**) and (**b**) 18-month-old (**b**) Prox1-GFP animals stained for α-SMA and Col4a. **c**, LECs along the LV and within the lymphatic valve can be visualized with Prox1-GFP. **d**, SMCs are α-SMA-positive. **e**, Col4a is a marker of the collagen basement membrane. Scale bars, 100 µm; $n = 5$ mice per group. **f**, Regions of interest (ROIs) were divided into valvular and perivalvular ROIs. **g**,**h**, Quantification of the percentage of area covered for Prox1 at the valve (**g**) and the perivalvular region (**h**). **i**–**l**, Area covered for α-SMA (**i** and **j**) and Col4a (**k** and **l**). **m**, LECs were quantified as being DAPI$^+$ and Prox1$^+$. **n**,**o**, Total number of DAPI$^+$ (**n**) and DAPI$^+$/Prox1$^+$ (**o**) cells did not decrease in 18-month-old animals compared to young animals. **p**, SMCs were considered DAPI$^+$/α-SMA$^+$ and were similarly abundant between young and old mice (**q**). Two-sided unpaired *t*-test was performed (**g**–**l**, **n**–**o** and **q**). Data are presented as the mean ± s.e.m.; $n = 5$ mice per group. **r**, Orientation of α-SMA and Col4a fibers. **s**, Fiber orientation in degrees for α-SMA$^+$ and Col4a$^+$ fibers in valvular and perivalvular ROIs. Orientation was computed as axial (0°) or longitudinal (+90° or −90°). **t**, Coherence of fiber orientation as a percentage for fibers in valvular and perivalvular ROIs. Scale bars, 100 µm. Two-way ANOVA with Sidak's multiple-comparison test was performed (**s** and **t**). Data are presented as the mean ± s.e.m.; $n = 5$ mice per group.

of contractile proteins in SMCs, and changes in the basement membrane[20,21]. Because aging is also associated with hyperplasia and dysmorphic LVs[18], we aimed to determine whether an age-dependent change in the structural components of LVs could drive biomechanical differences that would explain the observed flow changes in cLVs. We performed immunohistochemical staining of scLVs in 2-month-old and 18-month-old Prox1-GFP animals (Fig. 4a,b) to identify lymphatic endothelial cells (LECs; Fig. 4c), α-smooth muscle actin (α-SMA, Fig. 4d) for SMCs and collagen 4a (Col4a; Fig. 4e), a main structural protein of the lymphatic basement membrane. There was significant loss of Prox1 and α-SMA in both the lymphatic valve and the perivalvular regions of scLVs in aged mice. LECs (Prox1-positive area) covered around 12% less of the lymphatic valve in 18-month-old animals compared to young controls (97.2% ± 1.3% versus 85.8% ± 2.9%; $P = 0.0075$) and 74% less of the perivalvular portion of the LV (65.5% ± 3.3% versus 17.1% ± 3.1%, $P < 0.0001$). SMCs (α-SMA-positive area) covered 54% less of the valve (72.6% ± 7.1% versus 33.6% ± 5.1%, $P = 0.0021$) and 35% less of the perivalvular region (86.2% ± 3.5% versus 55.9% ± 5.2%, $P = 0.0013$; Fig. 4f–j).

A similar relationship for SMC coverage was noted in 22-month-old animals. α-SMA fluorescence was 37.5% lower in 22-month-old mice (97.5 ± 5.6 arb. units) compared to their young counterparts (156.1 ± 19.0 arb. units, $P = 0.0328$; Extended Data Fig. 3a,c), suggesting a debilitating loss in α-SMA and contractile ability. Interestingly, aging caused a 1.5-fold greater loss of SMC coverage at valves compared to perivalvular regions. Valvular α-SMA is thought to actively control valve leaflet movement in other rodent lymphatic chains, and its loss could increase reflux and decrease lymphatic efflux, as we observed in aged mice[35–37].

Quantification of the basement membrane thickness and Col4a expression showed no significant difference between 2-month-old and either 18-month-old or 22-month-old animals (Fig. 4k,l and Extended Data Fig. 3a,b), suggesting that the structural scaffolding of the scLVs is retained across aging. We then asked if the decreased expression of Prox1 and α-SMA was the result of either global cell loss or rather a cell-specific process. LECs are responsible for channeling flow, and SMCs drive spontaneous, phasic contractions in LVs. A reduction in either of these could decrease contractility. LECs were identified as $DAPI^+/Prox1^+$ cells, while SMCs were identified as being $DAPI^+/\alpha\text{-}SMA^+$[38]. Results showed that total cell, LEC and SMC numbers were comparable between 2-month-old and 18-month-old animals (total cell, $P = 0.3854$; LEC, $P = 0.9485$; SMA, $P = 0.7626$; Fig. 4m–q). We then asked if abnormal orientation of α-SMA and Col4a fibers could contribute to the anomalous contractility noted in aged animals (Fig. 4r). However, we found that fiber orientation and its coherence for both markers were preserved in aging (orientation: $P = 0.1539$; coherence: $P = 0.1466$; Fig. 4s,t). Together, these results show that reduced coverage of αSMA and Prox1, rather than fewer LECs or SMCs, could explain the reduced fluid transport seen in aged vessels. This decline in SMA expression also matches that seen in the nasopharyngeal lymphatic plexus[20] and mesenteric lymph vessels in aging[21], which might support the notion that this is a systemic process rather than a regionally specific event.

To further characterize scLV wall dynamics, we computed the average contraction amplitude over the systolic cycle (Extended Data Fig. 3d). We observed a 20% reduction in the contraction amplitude and a 30% longer contraction phase of 22-month-old vessels, compared to 2-month-old vessels ($P < 0.0001$; Extended Data Fig. 3d). Two-month-old scLVs achieved wall velocities double that of their aged counterparts ($P < 0.0001$; Extended Data Fig. 3e). In summary, our measurements suggest that reduced SMA fiber coverage, rather than basement membrane changes, coincides with slower and smaller intrinsic pulsations, which together with decreased contraction frequency (Fig. 2e) result in the lower average volumetric flow rates (Fig. 3d) in aging.

$PGF_{2\alpha}$ restores scLV pumping by improving LV contractility

Since intrinsic pulsations are the principal driver of cLV transport, and both LEC and SMC numbers are preserved in aged cLVs, we asked if it was possible to rescue the function of atrophic SMCs in aged scLVs and restore lymphatic drainage. We topically applied $PGF_{2\alpha}$, a prostanoid that induces LV contractions by increasing intracellular Ca^{2+} concentrations in SMCs[30,39,40] (Fig. 5a–d). $PGF_{2\alpha}$ increased the intrinsic pulsation rate (Fig. 5f) in young mice (50.7%, $P = 0.0216$) and even more in old mice (152.0%, $P = 0.0136$), restoring the intrinsic rate to levels seen in young animals before treatment ($P = 0.487$). Similarly, downstream speeds were increased in young mice (103.1%, $P = 0.0497$) and increased even more in old mice (3.5-fold, $P = 0.0020$), surpassing baseline speeds in young animals ($P = 0.016$; Fig. 5g). Notably, $PGF_{2\alpha}$ not only decreased the spatial median vessel diameter in 2-month-old ($P = 0.0327$) and 22-month-old ($P = 0.0329$; Fig. 5h) mice, but also increased the contraction amplitude (Δd; $P < 0.0001$ versus before; Fig. 5j), suggesting that in addition to increasing phasic activity it also enhances tonic activity. However, there was no change in the ejection rate in 2-month-old ($P = 0.1220$) or 22-month-old ($P = 0.8362$; Fig. 5i) mice, indicating that $PGF_{2\alpha}$ primarily stimulates SMC contractions but has no effect on valve dynamics. Reassuringly, topical application of $PGF_{2\alpha}$ did not induce changes in the cardiac or respiratory rates (Extended Data Fig. 4). These experiments confirmed that $PGF_{2\alpha}$ rescued the intrinsic pumping ability of aged vessels by amplifying the contractions and boosting their frequency. These observations further support the idea that age-induced cLV dysfunction can be reversed by optimizing SMC function.

To see if applying $PGF_{2\alpha}$ translated to improved cLV transport, we calculated volumetric flow rates and anterograde and retrograde fractions after treatment (Fig. 5e). We observed flow was predominantly unidirectional (Fig. 5e and Supplementary Videos 5 and 6). The anterograde fraction increased by 7.0% in 2-month-old mice (90.8% ± 0.8% versus 97.1% ± 0.6%, $P = 0.0045$) and by 31.7% in 22-month-old mice (72.5% ± 2.1% versus 95.5% ± 0.5%, $P = 0.0005$; Fig. 5l), while the retrograde fraction decreased by 64.2% in 2-month-old mice (8.1% ± 1.0% versus 2.9% ± 0.6%, $P = 0.0061$) and by 83.6% in 22-month-old mice (27.5% ± 2.1% versus 4.5% ± 0.4%, $P = 0.0005$; Fig. 5k). Average volumetric flow rates were significantly larger after $PGF_{2\alpha}$ in both 2-month-old mice (148.6%, $P = 0.0021$) and 22-month-old mice (181.4%, $P = 0.0215$; Fig. 5m). $PGF_{2\alpha}$ increased the anterograde fraction even when compared with untreated young controls ($P = 0.0012$ and $P = 0.0133$, respectively), implying that with adequate therapy, the function of aging LVs can be restored to youthful levels.

Restoring scLV function rescues CSF/ISF drainage in aged animals

Because cLVs drain CSF from the CNS, we asked whether restoring scLV function with $PGF_{2\alpha}$ would enhance CSF clearance. After intracisternal delivery of fluorescent microspheres, we quantified the number of particles detected in the scLVs as a surrogate of solute transport, as in Fig. 3e. CSF drainage in 2-month-old mice increased by 35.4% after administration of $PGF_{2\alpha}$ ($P = 0.0355$; Fig. 5n). Surprisingly, in aged mice treatment resulted in nearly four times more solute arriving to the cLN compared to untreated aged controls ($P = 0.0017$; Fig. 5n). cLV stimulation alone enhanced CSF drainage in aged mice above young untreated levels ($P = 0.0208$). Moreover, because cLVs transport fluid via bulk motion, increased CSF clearance should apply to all macromolecular solutes immersed in the fluid (for example, proteins and cells). To test whether $PGF_{2\alpha}$ could increase the efflux of proteins in the CSF, we injected ovalbumin conjugated to Alexa Fluor 647 (OVA-647) into the cisterna magna. Because 2P-OPTIC is only able to quantify transport along a single cLV, to include all scLVs we used an epifluorescence macroscope to quantify net transport of a protein-sized tracer (45 kDa) from the CSF. $PGF_{2\alpha}$ treatment was also extended to 60 min to determine if its effect could be sustained for longer durations. CSF clearance was inferred from changing fluorescence intensity of the OVA-647 tracer after cisterna magna injection (Fig. 6a and Supplementary Video 7). $PGF_{2\alpha}$ promoted robust CSF drainage in both young ($P < 0.0001$) and old ($P < 0.0001$; Fig. 6b,c) mice, and rescued the blunted CSF efflux in 22-month-old animals back to 2-month-old levels. Ex vivo analysis of the cLNs showed a significantly larger accumulation of OVA-647 after $PGF_{2\alpha}$ for 90 min in 2-month-old and 22-month-old mice (Extended Data Fig. 5).

Drainage of a protein tracer delivered into the cisterna magna can bypass the brain parenchyma, so to further evaluate the role of augmenting scLV transport on brain clearance, we labeled interstitial fluid (ISF) in the striatum by injecting Direct Blue 53 (DB53, also T-1824 or Evans Blue; Fig. 6a). DB53 was chosen because it is a small (960.8 Da), fluorescent tracer that reliably traces ISF. DB53 is cleared toward blood, where it has high affinity to plasma albumin, allowing it to remain in circulation for up to 135 min at stable concentrations[41–45]. Significantly less DB53 was retained in the brain after $PGF_{2\alpha}$ (6.3% ± 0.9% versus 10.1% ± 1.3%; $P = 0.0314$; Fig. 6d,e). Brain clearance can be quantified by assessing DB53 signal in the femoral vein, which was dramatically increased after $PGF_{2\alpha}$ compared with control ($P < 0.0001$; Fig. 6f,g). The DB53 signal was significantly higher with $PGF_{2\alpha}$ compared with

https://doi.org/10.1038/s43587-024-00691-3

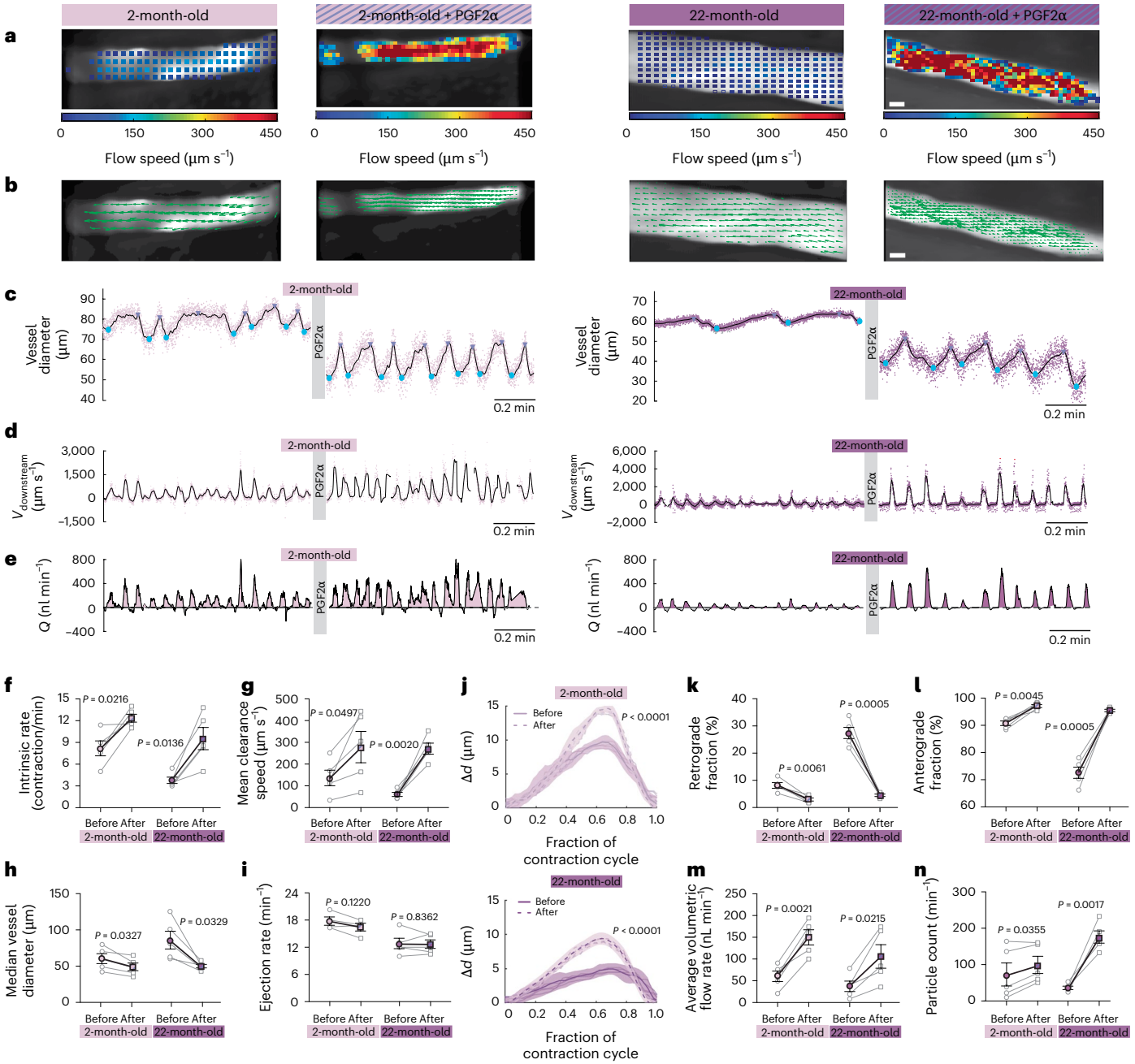

Fig. 5 | $PGF_{2\alpha}$ restores lymphatic flow and reverses the effects of aging on CSF drainage. a,**b**, Representative images of time-averaged speed (**a**) and velocity (**b**) in young mice and 22-month-old mice before (left column) and after (right column) $PGF_{2\alpha}$ administration. Scale bar, 50 µm. **c**,**f**,**j**, Vessel diameter variation shows that $PGF_{2\alpha}$ stimulates the vessel and promotes intrinsic pulsation for young and old groups (**c**), with a larger increase in intrinsic rate (**f**) and Δd (**j**) observed in old mice. **d**,**g**,**i**, Downstream velocity variation indicates that the $PGF_{2\alpha}$-induced stimulation of vessel walls increased efflux (d), with faster mean downstream speeds (**g**) and ejection rate (**i**). **e**, Temporal variation of instantaneous volume flow rate (Q) before and after administration of $PGF_{2\alpha}$ for young and old groups. **h**, Median vessel diameter indicates that administration of $PGF_{2\alpha}$ reduces the size of the vessel. Paired t-test was performed in **e**–**h**. Data are the mean ± s.e.m., $n = 5$. **k**, Retrograde fraction was decreased by $PGF_{2\alpha}$ for young and old group. **l**–**n**, Anterograde fraction (**l**), average volume flow rate (**m**) and particle count (**n**) were all restored by $PGF_{2\alpha}$ in aging. Two-sided paired t-test was performed (**f**–**i** and **k**–**n**). Two-way ANOVA with Sidak's multiple-comparisons test was performed (**j**). Data are presented as the mean ± s.e.m.; $n = 4$–5 mice per group.

control at 75 min (8.3 ± 1.3 versus 4.6 ± 0.8; $P = 0.0351$), 90 min (10.3 ± 1.5 versus 5.5 ± 0.6; $P = 0.0014$), 105 min (10.8 ± 1.4 versus 6.6 ± 0.7; $P = 0.0070$) and 120 min (11.45 ± 8.3 versus 6.8 ± 0.7; $P = 0.0023$; Fig. 6g). In summary, restoring scLV function boosts CSF/ISF drainage and increases the arrival of CNS-borne proteins to cLNs in both young and aged mice. These findings suggest that cervical lymphatics are important drivers of CSF clearance and function as critical bottlenecks in slowing CSF outflow in old age.

Discussion

In this study, we introduced 2P-OPTIC, a method to quantify cLV flow dynamics of CSF solutes. We presented a comparison of hydrodynamical measurements of cLVs in young and aged mice in vivo. We found that cLVs are ~70 µm in diameter and support flow speeds on the order of 150 µm s^{-1}. The primary driver of these viscosity-dominated flows is intrinsic contractions of the lymphangions, which are impaired by aging. As seen previously in other lymphatic networks[21], we found an

https://doi.org/10.1038/s43587-024-00691-3

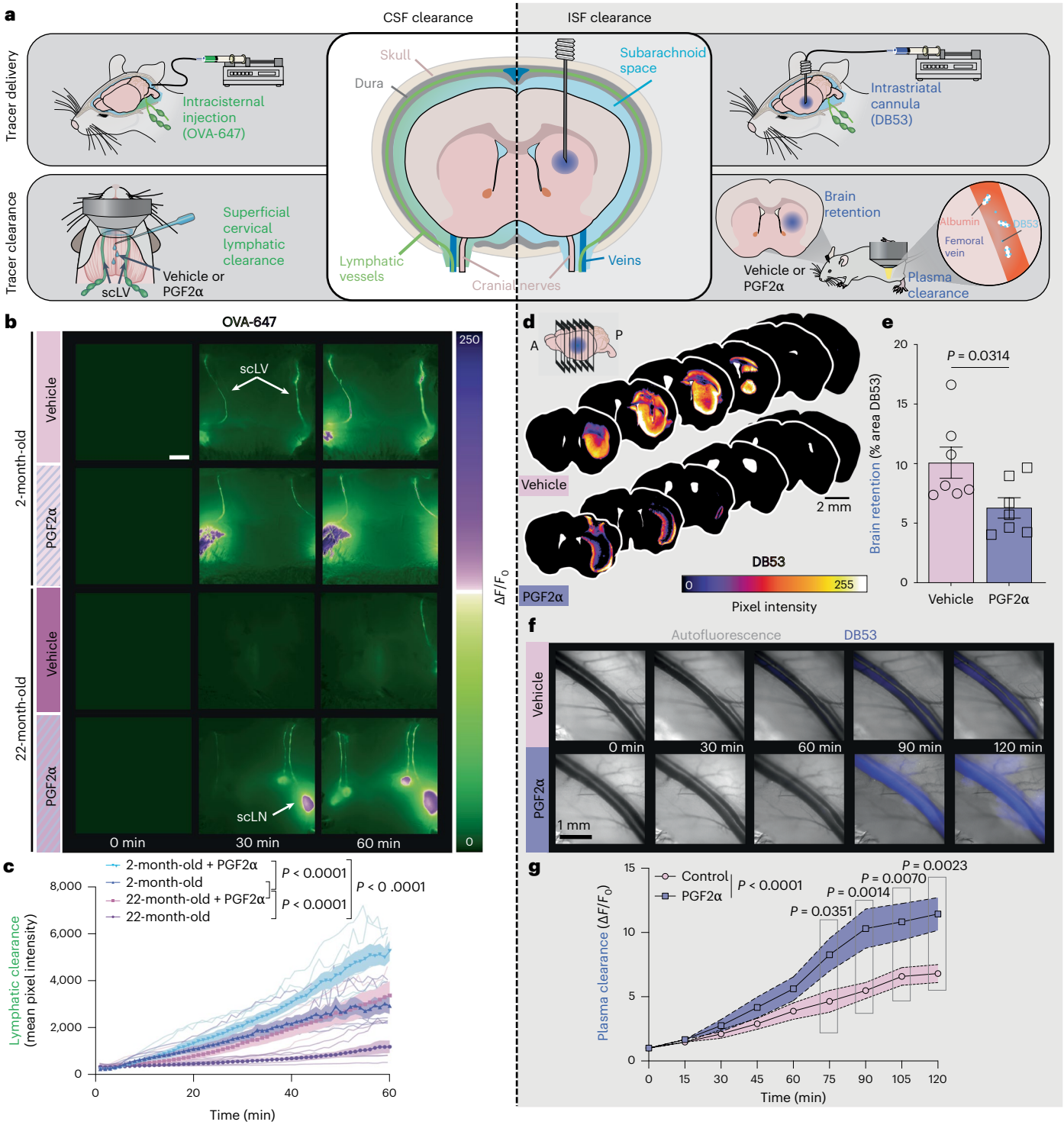

Fig. 6 | $PGF_{2\alpha}$ reverses the effects of aging on CSF drainage and increases brain clearance. a, CSF clearance was evaluated via an intracisternal injection of OVA-647, and CSF drainage was detected in scLVs with or without $PGF_{2\alpha}$ in young and old mice. **b**, Progressive increase in the mean fluorescence intensity measured for 60 min, indicating increased efflux after $PGF_{2\alpha}$. Scale bar, 2 mm. **c**, Quantification of mean pixel intensity for the 60-min in vivo imaging series depicted in **b**. Two-way ANOVA with Sidak's multiple-comparisons test. Data are presented as the mean ± s.e.m.; $n = 6–7$ mice per group. Clearance of ISF from the brain parenchyma was evaluated by injecting DB53 into the striatum. DB53 is cleared from the brain toward blood plasma, where it binds to circulating albumin and is retained for over 2 h, allowing stable quantification of brain clearance to plasma. **d**, Coronal sections from anterior (A) to posterior (P), showing brain retention of DB53 after intrastriatal injection. Scale bar, 2 mm. **e**, Quantification of brain retention expressed as the percentage area of DB53 fluorescence. Two-sided unpaired Student's *t*-test was performed. mean ± s.e.m., $n = 6–7$ mice per group. **f**, Representative imaging of the acquired in vivo femoral vein images after 1 µl 4% DB53 injection in the striatum. Scale bar, 1 mm. **g**, Quantification of plasma clearance measured at the femoral vein. Two-way ANOVA with Sidak's multiple-comparisons test was performed. Data are presented as the mean ± s.e.m.; $n = 6–7$ mice per group.

associated reduction in SMA[20,38] in lymphatic SMCs. Additionally, dysfunctional valves in aging scLVs failed to ensure unidirectional transport, further reducing efficiency of aging cLVs. The use of $PGF_{2\alpha}$, known to induce contractility of SMCs in the general circulation[30,46], restored pumping of scLVs by increasing intrinsic contractions without changing cardiac or respiration rates. Rescue of scLV function was evident in transport of lymph and in increased tracer accumulation in cLNs.

Unlike cardiovascular networks, lymphatic networks lack a central pump, so lymphatic fluid is transported by intrinsic contractions of the lymphangions and extrinsic contractions from surrounding skeletal or smooth muscle[23]. In both scLVs and dcLVs, we observed an average Re (<0.006) which is ~25% smaller than in rat mesenteric LVs, but typical for small LVs (<100 µm)[1]. Flow speeds during contractions increased nearly two orders of magnitude (~1,500 µm s^{-1}, instantaneous Re ~ 0.6), also comparable to rat mesenteric LVs[47]. Flow invariably remained laminar and viscosity-dominated. In scLVs, Wo ~ 0.03, indicating transient inertial effects are negligible. In contrast, Wo ~ 0.1 in rat mesenteric vessels[47], and Wo = 1.4 in the human thoracic duct, where inertial effects become important[48]. Interestingly, Re and Wo have comparable values in similarly sized blood vessels, and in brain perivascular spaces[49]. cLVs transported about a third of the flow (~70 nl min^{-1}) of rat mesenteric vessels with a similar diameter (91 µm, ~230 nl min^{-1})[50]. Flows oscillated at a frequency similar to the intrinsic contraction rate (~0.2 Hz ≈ 12 min^{-1}), like collecting LVs in the rat mesentery[51], but faster than abdominal LVs in mice (6 min^{-1})[40].

Our results show no cardiac or respiratory effects; the dominant flow frequency was an order of magnitude smaller than that of either (2–3 Hz). That finding is intuitive, since the scLVs sit near the skin and are relatively unconstrained by the neck musculature. Extrinsic pumping might matter more in dcLVs, surrounded by neck muscles. However, dependence on contractility renders cLVs vulnerable to aging. Aging results in morphological (for example, reduced vessel density) and functional (for example, reduced transport capacity) alterations in LVs, and lymphatic networks including thoracic duct, skin, meningeal and mesenteric LVs have shown impairment in aging[52]. Lower production of lymphangiogenic factors and diminished regenerative capacity of LECs are major causes. Aging also reduces SMA coverage around vessels and valves, and alters basement membranes, increasing permeability and decreasing contractility[35,51,53–55]. Our study shows that cLVs are affected by the same changes as those seen in other collecting LVs.

Our study shows that cLVs facilitate CSF drainage and are important for the proposed glymphatic–lymphatic system. The glymphatic system transports CSF through arterial perivascular spaces into the brain's extracellular space, where it mixes with interstitial fluid and metabolic waste, subsequently draining along perivenous spaces[56,57]. Arachnoid cuff exit (ACE) points allow direct exchange of fluids and solutes between the subarachnoid space and the dura, enabling efflux via meningeal lymphatics[58] or cranial and spinal nerves, where it is taken up by the nasopharyngeal lymphatic plexus[20] and extracranial collecting LVs, which drain into cLNs via cLVs[7,59–61]. Thus, cLVs are pivotal for CNS clearance[60], as highlighted by the fact that knocking out *Prox1* (thereby causing mispatterned and leaky LVs) and/or ligating cLVs reduced CSF entry into the glymphatic pathway and slowed CSF clearance[9]. Reducing flow downstream (in the lymphatics) limits flow upstream (glymphatic) due to conservation of mass. Optically ablating meningeal lymphatics had a similar effect[9]. While we demonstrate that aging drastically affects scLVs, aging also affects meningeal LVs, further hindering CSF drainage[9,18]. Aging also reduces CSF production[62] and outflow from cranial foramina[7,18,63]. Nonetheless, our study shows that restoring scLV function alone is sufficient to rescue these age-induced effects, offering a treatment strategy.

Reestablishing CSF clearance has been proposed as therapy for Alzheimer's disease, Parkinson's disease, ischemic stroke and traumatic brain injury[64]. Meningeal LVs in aged mice can be rescued with vascular endothelial growth factor-C (VEGF-C), improving glymphatic flow and cognition in old mice[9]. This interaction is mediated by cLVs because their ligation abolished the benefits[9]. Ablating meningeal LVs increases amyloid-β burden and promotes deposition in mouse models of Alzheimer's disease[9], while mice that lack meningeal lymphatics also retain more tau[65], likewise associated with Alzheimer's disease. Aged animals clear an intraparenchymal injection of radio-labeled amyloid-β at a 40% slower rate[66]. Similarly, ligation of cLVs restricted lymphatic efflux and exacerbated the aggregation of α-synuclein in mouse models of Parkinson's disease[11]. In the case of acute ischemic stroke, mice with dysfunctional meningeal LVs have increased infarct volumes after transient middle cerebral artery occlusion[12].

Besides affecting disease, cLVs also modulate therapies. For example, meningeal LVs undergo extensive remodeling in mouse models of intracranial gliomas and metastatic melanoma, decreasing dendritic cell trafficking to cLNs, dampening $CD8^+$ responses, and reducing the effect of anti-PD-1/CTLA-4 checkpoint therapy[16,67]. Restoring LVs with VEGF-C improves the response to immune checkpoint inhibitors targeted at CNS tumors and anti-amyloid antibodies used in the treatment of Alzheimer's disease[16,67,68]. We show that scLVs can rescue ISF and CSF drainage in aged mice by topical application of $PGF_{2\alpha}$ (dinoprost), a naturally occurring prostanoid that binds to the $PGF_{2\alpha}$ receptor. An analog of $PGF_{2\alpha}$ (carboprost) is used clinically to induce uterine contractions and terminate postpartum bleeding[69]. Carboprost is injected intramuscularly[70] but could be administered transdermally in the neck, which is less invasive than VEGF-C gene therapy or hydrogel-encapsulated VEGF-C application to the skull (some of which are in clinical trials; NCT03658967)[52]. Small concentrations of phenylephrine (10 nM) applied to dcLVs also enhance CSF drainage[20]. Both $PGF_{2\alpha}$ and phenylephrine are G_q-protein-coupled receptor ligands, possibly suggesting overlapping mechanisms. Sodium nitroprusside (3 µM), a nitric oxide donor, also increased tracer uptake in deep cervical lymph nodes (dcLNs), suggesting that other modulations are possible[20]. However, clearance of CSF tracers toward the dcLNs increased more with $PGF_{2\alpha}$ than with either phenylephrine or nitroprusside (approximately 180% versus 51.6% versus 33.9%, respectively) compared to control groups. Thus, modulating scLV function can augment CSF drainage without access to dcLVs.

2P-OPTIC provides quantitative, real-time, in vivo measurements of CSF drainage via cLVs. Prior studies focused on ex vivo explants of LVs that were cannulated and pressurized. While those techniques allow detailed observation, they remove the LVs from surrounding tissue. Prior studies measured lymphatic flows in vivo with ultrasound[24,25] or optical coherence tomography[71,72] but were generally not compatible with fluorescent reporters (for example, Prox1-GFP). Some studies measured cLV kinetics using fluorescence stereomicroscopy to evaluate perineural outflow and draining lymphatics[7,20,73]. While those methods allow large imaging volumes and robust tracer quantification (Fig. 6b), they generally equate fluorescence intensity with fluid transport, which our study suggests correlates more with LV diameter than flow speed. A recent study[20] found that higher doses of phenylephrine (50 µM–5 mM) cause tonic constriction of dcLVs resulting in decreased LV diameter and lower fluorescence intensity of an intraluminal tetramethylrhodamine-dextran, while sodium nitroprusside (25 µm) relaxed dcLVs, enlarging vessels and increasing fluorescence intensity. Intriguingly, either phenylephrine or nitroprusside decreased apparent drainage to dcLNs, suggesting that fluorescence intensity in dcLVs might not reliably predict transport. Two-photon microscopy overcomes limitations of stereomicroscopy by allowing in vivo imaging with high resolution, small depth of focus and detection of multiple fluorophores. Previous approaches have used two-photon microscopy to track endogenous lymphocytes[33,50,74,75], but their interactions with the LV wall limit their ability to track bulk fluid motion[33,74,75]. 2P-OPTIC uses a dual tracer approach, labeling cLVs to track contractions and using microspheres to measure flow. Disadvantages of this technique are the need to inject exogenous tracers and surgically

expose LVs; however, in the future, the technique will be optimized by labeling endogenous components of lymph (that is, expressed proteins) and using transdermal two-photon imaging. While 2P-OPTIC was developed for cLVs, it can be used in other lymphatic networks.

In conclusion, we developed two-photon optical imaging with particle tracking in vivo (2P-OPTIC) and found that cervical lymphatic pumping is impaired in aging. Aging reduced the frequency and amplitude of lymphatic contractions, slowing flow. Aged lymphatic valves failed to open and close properly, consistent with a loss of SMC coverage, explaining the increase in retrograde flow. Because multiple CSF outflow pathways converge at cLVs, our results provide evidence that improving cLV function can restore CSF drainage in aged animals and possibly provide a therapeutic platform for treating neurological diseases.

Methods

Animals

Animal experiments were approved by the University Committee on Animal Resources of the University of Rochester and followed the National Institutes of Health (NIH) Guide for the Care and Use of Laboratory Animals and the ARRIVE Guidelines. Male C57BL/6 8-week-old mice were obtained from Charles River Laboratories. Eighteen-month-old and 22-month-old mice were acquired from the National Institute on Aging. Prox1-EGFP^{+} reporter mice were kindly provided by K. Alitalo on the C57BL/6JRj background (Janvier Labs) were utilized[76]. Mice were housed at an ambient temperature of 70–74 °F and a humidity of 30–70%. For different experimental groups, the number of mice was based on our experience, types of technical difficulties and previously published studies. Mice were allocated to different experimental groups randomly.

Drugs

Animals were anesthetized with ketamine–xylazine (100/10 mg kg^{-1}, intraperitoneally). $PGF_{2\alpha}$ (5 µM in PBS, VWR) was applied directly onto the cervical lymph vessel.

Surgical procedure

Anesthetized mice were placed in a stereotaxic frame and a 30-gauge needle connected to PE-10 tubing filled with artificial CSF (aCSF) was inserted into the cisterna magna as described here[77]. Then, animals were positioned on their backs on a heating pad to maintain body temperature. A midline surgical incision was made from the chin to the sternum to expose the scLV. To expose dcLVs, the superficial cervical fascia was incised and a deep neck dissection along the lateral border of the trachea was achieved by separating along the medial border of sternocleidomastoid and posterior belly of the digastric muscles to expose the common carotid artery and internal jugular vein. dcLVs run superficial to both these vascular structures and were confirmed as being Prox1-GFP positive. Afterwards, FITC–dextran (3 kDa, 1% solids in saline, 20 µl, Invitrogen) was injected in each cheek. Red fluorescent polystyrene microspheres (FluoSpheres 1.0 µm, 580/605 nm, 0.25% solids in aCSF (Invitrogen) were briefly sonicated and infused at 2 µl min^{-1} for 5 min into the cisterna magna catheter with a syringe pump (Harvard Apparatus).

Measurement of vital signs

Heart and respiratory rate were measured using a small-animal physiological monitoring device (Harvard Apparatus), which acquired measurements at 1 kHz and 250 Hz, respectively. The signals were digitized and recorded with a DigiData 1550A digitizer and AxoScope software (Axon Instruments).

In vivo two-photon laser scanning microscopy

A resonant scanner B scope (Thorlabs) with a Chameleon Ultra II laser (Coherent) was used for two-photon imaging. FITC–dextran and red microspheres were excited at a wavelength of 820 nm. A water immersion ×20 objective (1.0 NA, Olympus) was used. Images were acquired at 60 Hz (ThorImageLS software) simultaneously with physiological recordings (3 kHz, ThorSync software).

Image processing

The 16-bit images were obtained from two-photon microscopy using two channels (red and green), each with spatial dimensions of 256 × 256 at least. The green channel captured the FITC–dextran in the lymph vessel, while the red channel captured the fluorescent microspheres flowing in the lymph vessel. Image registration was the first step in imaging processing, necessary to account for movement of the mouse in the background. An efficient algorithm in MATLAB[78] was used to apply rigid translations (no rotation or deformation) that were calculated to an accuracy of 0.2 pixels. At least ten continuous images from the recording that showed the most stability and least movement were used as a reference for the rigid translations. Erroneous correlations in the translations (where the algorithm failed) were inspected and manually corrected via linear interpolation. The corrected translations were then sequentially applied to the images whose edges are also padded with zero-value pixels to ensure spatial homogeneity across all images without modifying the image resolution. Particles were then detected in each image by applying a minimum intensity threshold. These particles are typically resolved across 3–4 pixels in the image with an image resolution of 1.29 µm per pixel. The motion artifact index was calculated from time-lapse imaging using an epifluorescence macroscope. Dissimilarity between sequential images was computed as the mean of the absolute value of the difference of each pixel.

Particle tracking velocimetry

The particles detected in each image were tracked using an automated particle tracking velocimetry routine implemented in MATLAB[79,80]. Briefly, the algorithm locates each particle with a sub-pixel accuracy and correlates its movement across images to obtain a series of particle locations (particle tracks) for the duration of the recording. The particle velocities are then calculated by convolution with a Gaussian smoothing and differentiation kernel. Stagnant particles that had adhered to the wall of the lymph vessel, and hence no longer follow lymph flow, were masked in each image by subtracting a dynamic background image. This image was different for each frame and was computed by taking the average of 100 frames before and after the given image.

Lymph vessel diameter and contraction frequency

Vessel diameter. Using a custom MATLAB code, the spatial median vessel diameter was measured for the same temporal segments used for speed measurement. First, the centerline of the imaged vessel was identified by an algorithm that applied a spatially varying threshold for each image, then identified the edge, using the 'skeletonize' function in MATLAB. The identified centerline was also verified manually. Twenty transverse lines were then interpolated and the changes in the vessel diameter were measured with sub-pixel accuracy by identifying locations along the transverse lines where the pixel intensity dropped to 20–40% of the maximum value. Then, the median over space and time was computed. Any small systematic drift in the median value (due to translation of the two-photon imaging plane or movement in and out of the imaging plane due to respiration artifacts) was smoothed by computing a moving average over a 1-s window.

Intrinsic pulsation rate. The MATLAB function 'findpeaks' was used to identify the maxima and minima of the smoothed vessel diameter measurements obtained above. Contractions of amplitude less than 3% of the mean diameter or those separated by less than 2 s were rejected. The mean values of maxima and minima were then identified in 4–5 one-minute time windows, and the average value of the two means was assigned as the contraction frequency per minute.

Computing flow-derived quantities

Mean clearance speed. Five-minute recording segments were manually selected for analyses to ensure uninterrupted continuous particle count in each frame. Mean clearance speeds were obtained by segregating the imaged domain into bins of size 5 or 10 pixels (depending on particle counts), computing the time-averaged flow velocity in each bin, and then computing the spatial average. We used at least 30 separate measurements in space with each at least 7 measurements in each bin to ensure reliable estimates of the mean.

Downstream velocity. We computed the spatially averaged mean downstream velocity, $V_{\text{downstream}}$, in each frame using the relationship $V_{\text{downstream}} = u \cdot \bar{u}_{avg}$, where u is the instantaneous particle velocity and $\bar{u}_{\text{avg}}$ is the field of unit vectors computed from the time-averaged flow field in the direction of lymphatic fluid efflux from vessel.

Ejection rate. The ejection rate was calculated as pulsation frequency (min^{-1}) of the downstream velocity. The ejection rate reported for each dataset was the average number of oscillations measured in at least three nonoverlapping 1-min intervals.

Instantaneous volumetric flow rate, anterograde fraction, retrograde fraction and average volumetric flow rate. The instantaneous volumetric flow rate, Q, for each frame was computed as the product of the measured downstream velocity $V_{\text{downstream}}$ and the approximate cross-sectional area of the vessel, $\pi D^2/4$, where D is the measured spatial median vessel diameter in each frame. A positive value of Q indicates lymphatic fluid ejection from the vessel (anterograde flow) and a negative value indicates retrograde flow. The volumetric flow rate was computed for 1-min time windows in the recording. The area under this curve was computed in MATLAB to determine volume flow rate-related quantities. The total positive area indicates the volume of lymph ejected from the vessel, and the negative area (area of curve below zero) indicates the volume of lymph that flows into the lymphangion upstream of the imaged section. The ejection fraction is calculated as the percentage of the flow in the forward direction (the ratio of total positive flow volume to the total volume flowing through the lymphangion), and the retrograde fraction is calculated as the percentage of flow volume that flows upstream (the ratio of total volume to the total volume flowing through the lymphangion). The net volume or average volumetric flow rate cleared from the vessel was calculated as the difference between the total positive and negative flow volumes in a 1-min window.

Immunohistochemistry

Mice were transcardially perfused with 4% paraformaldehyde in 0.1 M phosphate buffer, pH 7.4, and the cervical lymph vessels were carefully dissected under a dissection macroscope and placed over slides coated with a solution of gelatin and chromium potassium sulfate dodecahydrate. The vessels, while still attached to their respective nodes, were incubated in 24-well microtiter plates (Corning) in blocking solution of 10% serum-PBS containing 0.1% Triton X-100, 0.05 mg ml^{-1} Affinipure Fab fragment (Jackson ImmunoReseach), 0.2% gelatin for 2 h at room temperature, followed by three 5-min washes in PBS. The vessels were incubated using the mesh well inserts that allowed the entire sample (vessels attached to the nodes) to be incubated and washed by blocking solution. Incubations with the primary antibodies for SMA (1:250 dilution; A5228, Millipore Sigma), collagen IV (1:400 dilution; 2150-1470, Bio-Rad) and LEC marker LYVE1 (1:400 dilution; 25-0443-82, Invitrogen) were carried out overnight at 4 °C in PBS containing 5% normal donkey serum, 0.1% Triton X-100 and 0.2% gelatin under agitation. After PBS washing, tissues were incubated with a mixture of secondary antibodies Cy3-conjugated donkey anti-rabbit, Cy-2 conjugated donkey anti-rabbit and Cy5-conjugated donkey anti-mouse (1:500 dilution; Jackson ImmunoResearch; 711165152 and 715175151, respectively) and DAPI (2.5 μg ml^{-1}; D21490, Invitrogen) in PBS containing 5% normal donkey serum, 0.1% Triton X-100 and 0.2% gelatin for 1 h at room temperature. PBS-washed samples were then mounted on microscope slides in wells created with adhesive spacers. The LVs were unfurled from the respective nodes and were mounted with ProLong Gold Antifade Mount (P36930, Invitrogen). The immunolabeled lymph vessels were imaged using confocal microscopy (FV3000RS, Olympus). Multichannel z-stacks (×20, 1 μm step size) across the total width of the lymph nodes were acquired using the same acquisition parameters for all samples. To evaluate protein distribution, the central plane of the acquired z-stacks was analyzed using the plot profile function of ImageJ (version 1.53c, NIH), drawing a 200-μm-wide line perpendicular to the vessel lumen, obtaining the linear distribution of fluorescence. Due to the variability of the lymph vessel width, the x axis of the obtained graphs was normalized by its own diameter. The resulting distributions displayed the raw fluorescence distribution on the y axis and width ratio on the x axis, allowing their direct comparison. To evaluate differences in protein expression, the area under the curve was calculated for all samples and both proteins. Coverage area was calculated by using an automated thresholding step and computing the percentage of pixels within a LV ROI that was manually drawn. Prox1-GFP images were used to generate ROIs. The valvular region was identified as a Prox1-GFP dense region corresponding to the two semilunar leaflets that form the lymphatic valve. The prevalvular and postvalvular regions of the LV were defined as the regions immediately proximal and distal to the valve within the ×40 magnification image (field of view: 318.20 μm × 318.20 μm). These two regions were combined to generate a perivalvular ROI. DAPI^+ nuclei were counted using CellCounter on Fiji. To quantify LECs, DAPI^+ cells that were also Prox1^+ were considered LECs. LECs were expressed as a percentage of all DAPI^+ nuclei. SMCs were quantified from DAPI^+ channel images where LEC nuclei were subtracted. Remaining DAPI^+ nuclei that also stained positive for SMA were considered SMCs and expressed as a percentage of DAPI^+ nuclei. Fiber orientation was computed using OrientationJ on Fiji[81]. Since orientations ranged from −90° to 90° but functionally have a longitudinal orientation, we calculated the absolute value of all negative orientations and expressed orientation in the range of 0–90°. The OrientationJ plugin also calculates coherence of fiber orientation, and this was also evaluated for both valvular and perivalvular ROIs. Representative videos were generated from confocal high-magnification z-stacks (×60, 0.4 μm step size, FV3000RS, Olympus) acquired with identical parameters.

Epifluorescence optical microscopy

OVA-647 (0.5% wt/vol, 45 kDa, Invitrogen, 10 μl, 2 μl min^{-1}) was injected into the cisterna magna through a 30-gauge needle connected to PE-10 tubing using a syringe pump (Harvard Apparatus). cLVs were surgically exposed as before and imaged using a fluorescence macroscope (MVX10, Olympus) with a PRIOR Lumen 1600-LED light source and an ORCA Flash 4.0 digital camera (Hamamatsu) using Metamorph software. The images at ×20 magnification from the far-red emission channel (647 nm) were collected at 1-min intervals for 60 min following the start of the injection. Exposure time was kept constant across all the experimental groups. One microliter of PBS with or without 5 μM $\text{PGF}_{2\alpha}$ was applied directly onto the cervical lymph vessel simultaneously with the injection of OVA-647 into the cisterna magna.

Lymph node imaging

One microliter of PBS with or without 5 μM $\text{PGF}_{2\alpha}$ was applied directly onto the cervical lymph vessel simultaneously with the injection of OVA-647 (0.5% wt/vol, 45 kDa, Invitrogen, 10 μl, 2 μl min^{-1}) into the cisterna magna for 90 min. Then, the superficial and deep cLNs were dissected and put on the microscope slices (Fisherbrand). The lymph nodes were placed under the microscope (MVX10 Research Macro

Zoom Microscope, Olympus). The images were acquired in the far-red emission channel (647 nm).

Clearance assay

A clearance assay was conducted using our published method[41]. Briefly, anesthetized mice were mounted in a stereotaxic apparatus and a small burr hole was made (AP +0.6 mm; ML −2.0 mm). A guide cannula (26 G, C315G SPC, 4.5 mm below pedestal) and dummy cannula (33 G, C315DC/SP, 0.1 mm projection) was placed at DV 3.3 mm. After 48 h, the dummy cannula was replaced by the inner cannula (33 G, C315I/SP, 0.1 mm projection), connected by a PE-10 tubing to a 10 µl Hamilton syringe containing 4% (wt/vol) DB53 in sterile aCSF. The left femoral vein was exposed via skin resection and was placed under a fluorescence macroscope (microscope: MVX10, Olympus; light: PRIOR Lumen 1600-LED; camera: Flash 4.0 digital, Hamamatsu). The pump infusion (1 µl, 0.2 µl min^{-1}) was triggered simultaneously with the imaging over the vein, once every 15 min for 2 h for the intraparenchymal delivery. PBS (1 µl) with or without 5 µM $PGF_{2\alpha}$ was applied directly onto the bilateral scLVs for the duration of the imaging. At the end of the experiment, animals were decapitated, and their brains were harvested for postmortem analysis. Quantitative analysis of the femoral vein and ex vivo brain imaging data has been described in a previous paper[41].

Statistics and reproducibility

All statistical analyses were performed using GraphPad Prism 8 and/or MATLAB. Tests were chosen based on the dataset and are reported in the figure legends. The analysis methods include two-way ANOVA with Sidak's multiple-comparisons test, one-way ANOVA with Tukey's multiple-comparisons test, and two-sided paired *t*-test. $P < 0.05$ was considered statistically significant. All data are presented as the mean ± s.e.m. No statistical methods were used to predetermine sample sizes but our sample sizes are similar to those reported in previous publications[17,49,82]. Data distribution was assumed to be normal, but this was not formally tested. Data collection and analysis were not performed blind due to the conditions of the experiments. Animals or data points were excluded from the study either if the image registration algorithm implemented in the study failed due to excessive motion artifacts or if the anesthesia paradigm failed.

Reporting summary

Further information on research design is available in the Nature Portfolio Reporting Summary linked to this article.

Data availability

Source data are provided with this paper. All other data supporting the findings of this study are available from the corresponding authors upon reasonable request.

Code availability

All relevant code is available in the public domain repository at https://gitlab-public.circ.rochester.edu/araghuna/bulk-flow-is-not-an-artifact_raghunandan_et_al_2021.git/.

References

1. Moore, J. E. Jr. & Bertram, C. D. Lymphatic system flows. *Annu. Rev. Fluid Mech.* **50**, 459–482 (2018).
2. Swartz, M. A. The physiology of the lymphatic system. *Adv. Drug Deliv. Rev.* **50**, 3–20 (2001).
3. Louveau, A. et al. Structural and functional features of central nervous system lymphatic vessels. *Nature* **523**, 337–341 (2015).
4. Aspelund, A. et al. A dural lymphatic vascular system that drains brain interstitial fluid and macromolecules. *J. Exp. Med.* **212**, 991–999 (2015).
5. Goldmann, J. et al. T cells traffic from brain to cervical lymph nodes via the cribroid plate and the nasal mucosa. *J Leukoc. Biol.* **80**, 797–801 (2006).
6. Louveau, A. et al. Understanding the functions and relationships of the glymphatic system and meningeal lymphatics. *J. Clin. Invest.* **127**, 3210–3219 (2017).
7. Ma, Q., Ineichen, B. V., Detmar, M. & Proulx, S. T. Outflow of cerebrospinal fluid is predominantly through lymphatic vessels and is reduced in aged mice. *Nat. Commun.* **8**, 1434 (2017).
8. Cserr, H. F., Harling-Berg, C. J. & Knopf, P. M. Drainage of brain extracellular fluid into blood and deep cervical lymph and its immunological significance. *Brain Pathol.* **2**, 269–276 (1992).
9. Da Mesquita, S. et al. Functional aspects of meningeal lymphatics in ageing and Alzheimer's disease. *Nature* **560**, 185–191 (2018).
10. Wang, L. et al. Deep cervical lymph node ligation aggravates AD-like pathology of APP/PS1 mice. *Brain Pathol.* **29**, 176–192 (2019).
11. Zou, W. et al. Blocking meningeal lymphatic drainage aggravates Parkinson's disease-like pathology in mice overexpressing mutated α-synuclein. *Transl. Neurodegener.* **8**, 7 (2019).
12. Yanev, P. et al. Impaired meningeal lymphatic vessel development worsens stroke outcome. *J. Cereb. Blood Flow Metab.* **40**, 263–275 (2020).
13. Bolte, A. C. et al. Meningeal lymphatic dysfunction exacerbates traumatic brain injury pathogenesis. *Nat. Commun.* **11**, 4524 (2020).
14. Liu, X. et al. Subdural haematomas drain into the extracranial lymphatic system through the meningeal lymphatic vessels. *Acta Neuropathol. Commun.* **8**, 16 (2020).
15. van Zwam, M. et al. Brain antigens in functionally distinct antigen-presenting cell populations in cervical lymph nodes in MS and EAE. *J. Mol. Med.* **87**, 273–286 (2009).
16. Song, E. et al. VEGF-C-driven lymphatic drainage enables immunosurveillance of brain tumours. *Nature* **577**, 689–694 (2020).
17. Hussain, R. et al. Potentiating glymphatic drainage minimizes post-traumatic cerebral oedema. *Nature* **623**, 992–1000 (2023).
18. Ahn, J. H. et al. Meningeal lymphatic vessels at the skull base drain cerebrospinal fluid. *Nature* **572**, 62–66 (2019).
19. Zhou, Y. et al. Impairment of the glymphatic pathway and putative meningeal lymphatic vessels in the aging human. *Ann. Neurol.* **87**, 357–369 (2020).
20. Yoon, J. H. et al. Nasopharyngeal lymphatic plexus is a hub for cerebrospinal fluid drainage. *Nature* **625**, 768–777 (2024).
21. Zolla, V. et al. Aging-related anatomical and biochemical changes in lymphatic collectors impair lymph transport, fluid homeostasis, and pathogen clearance. *Aging Cell* **14**, 582–594 (2015).
22. Cserr, H. F. & Knopf, P. M. Cervical lymphatics, the blood-brain barrier and the immunoreactivity of the brain: a new view. *Immunology Today* **13**, 507–512 (1992).
23. Zawieja, D. C. Contractile physiology of lymphatics. *Lymphat. Res. Biol.* **7**, 87–96 (2009).
24. Naito, T. et al. New method for evaluation of lung lymph flow rate with intact lymphatics in anaesthetized sheep. *Acta Physiol.* **188**, 139–149 (2006).
25. Onizuka, M., Flatebo, T. & Nicolaysen, G. Lymph flow pattern in the intact thoracic duct in sheep. *J. Physiol.* **503**, 223–234 (1997).
26. Proulx, S. T. et al. Use of a PEG-conjugated bright near-infrared dye for functional imaging of rerouting of tumor lymphatic drainage after sentinel lymph node metastasis. *Biomaterials* **34**, 5128–5137 (2013).
27. Davis, M. J. et al. Modulation of lymphatic muscle contractility by the neuropeptide substance P. *Am. J. Physiol. Heart Circ. Physiol.* **295**, H587–H597 (2008).

28. Margaris, K. N., Nepiyushchikh, Z., Zawieja, D. C., Moore, J. Jr. & Black, R. A. Microparticle image velocimetry approach to flow measurements in isolated contracting lymphatic vessels. *J. Biomed. Opt.* **21**, 25002 (2016).
29. Johnston, M. G., Kanalec, A. & Gordon, J. L. Effects of arachidonic acid and its cyclo-oxygenase and lipoxygenase products on lymphatic vessel contractility in vitro. *Prostaglandins* **25**, 85–98 (1983).
30. Ohhashi, T. & Azuma, T. Variegated effects of prostaglandins on spontaneous activity in bovine mesenteric lymphatics. *Microvasc. Res.* **27**, 71–80 (1984).
31. Johanson, C. E. et al. Altered formation and bulk absorption of cerebrospinal fluid in FGF-2-induced hydrocephalus. *Am. J. Physiol.* **277**, R263–R271 (1999).
32. Bachmann, S. B., Proulx, S. T., He, Y., Ries, M. & Detmar, M. Differential effects of anaesthesia on the contractility of lymphatic vessels in vivo. *J. Physiol.* **597**, 2841–2852 (2019).
33. Sarimollaoglu, M. et al. High-speed microscopy for in vivo monitoring of lymph dynamics. *J. Biophotonics* **11**, e201700126 (2018).
34. Davis, M. J., Rahbar, E., Gashev, A. A., Zawieja, D. C. & Moore, J. E. Jr. Determinants of valve gating in collecting lymphatic vessels from rat mesentery. *Am. J. Physiol. Heart Circ. Physiol.* **301**, H48–H60 (2011).
35. Bridenbaugh, E. A. et al. Lymphatic muscle cells in rat mesenteric lymphatic vessels of various ages. *Lymphat. Res. Biol.* **11**, 35–42 (2013).
36. Kataru, R. P. et al. Structural and functional changes in aged skin lymphatic vessels. *Front. Aging* **3**, 864860 (2022).
37. Scallan, J. P., Zawieja, S. D., Castorena-Gonzalez, J. A. & Davis, M. J. Lymphatic pumping: mechanics, mechanisms and malfunction. *J. Physiol.* **594**, 5749–5768 (2016).
38. Dostovic, Z., Dostovic, E., Smajlovic, D., Ibrahimagic, O. C. & Avdic, L. Brain edema after ischaemic stroke. *Med. Arch* **70**, 339–341 (2016).
39. Suematsu, E., Resnick, M. & Morgan, K. G. Change of Ca^{2+} requirement for myosin phosphorylation by prostaglandin F2 alpha. *Am. J. Physiol.* **261**, C253–C258 (1991).
40. Chong, C. et al. In vivo visualization and quantification of collecting lymphatic vessel contractility using near-infrared imaging. *Sci. Rep.* **6**, 22930 (2016).
41. Pla, V. et al. A real-time in vivo clearance assay for quantification of glymphatic efflux. *Cell Rep.* **40**, 111320 (2022).
42. Freedman, F. B. & Johnson, J. A. Equilibrium and kinetic properties of the Evans blue-albumin system. *Am. J. Physiol.* **216**, 675–681 (1969).
43. Wolman, M. et al. Evaluation of the dye-protein tracers in pathophysiology of the blood-brain barrier. *Acta Neuropathol.* **54**, 55–61 (1981).
44. Yao, L., Xue, X., Yu, P., Ni, Y. & Chen, F. Evans blue dye: a revisit of its applications in biomedicine. *Contrast Media Mol Imaging* **2018**, 7628037 (2018).
45. Yen, L. F., Wei, V. C., Kuo, E. Y. & Lai, T. W. Distinct patterns of cerebral extravasation by Evans blue and sodium fluorescein in rats. *PLoS ONE* **8**, e68595 (2013).
46. Ohhashi, T., Kawai, Y. & Azuma, T. The response of lymphatic smooth muscles to vasoactive substances. *Pflugers Arch* **375**, 183–188 (1978).
47. Dixon, J. B. et al. Lymph flow, shear stress, and lymphocyte velocity in rat mesenteric prenodal lymphatics. *Microcirculation* **13**, 597–610 (2006).
48. Rahbar, E. & Moore, J. E. Jr. A model of a radially expanding and contracting lymphangion. *J. Biomech.* **44**, 1001–1007 (2011).
49. Mestre, H. et al. Flow of cerebrospinal fluid is driven by arterial pulsations and is reduced in hypertension. *Nat. Commun.* **9**, 4878 (2018).
50. Dixon, J. B., Zawieja, D. C., Gashev, A. A. & Cote, G. L. Measuring microlymphatic flow using fast video microscopy. *J. Biomed. Opt.* **10**, 064016 (2005).
51. Zawieja, D. C., Davis, K. L., Schuster, R., Hinds, W. M. & Granger, H. J. Distribution, propagation, and coordination of contractile activity in lymphatics. *Am. J. Physiol.* **264**, H1283–H1291 (1993).
52. Gonzalez-Loyola, A. & Petrova, T. V. Development and aging of the lymphatic vascular system. *Adv. Drug Deliv. Rev.* **169**, 63–78 (2021).
53. Muthuchamy, M., Gashev, A. A., Boswell, N., Dawson, N. & Zawieja, D. C. Molecular and functional analyses of the contractile apparatus in lymphatic muscle. *FASEB J.* **17**, 920–922 (2003).
54. Akl, T. J., Nagai, T., Coté, G. L. & Gashev, A. A. Mesenteric lymph flow in adult and aged rats. *Am. J. Physiol. Heart Circ. Physiol.* **301**, H1828–H1840 (2011).
55. Nagai, T., Bridenbaugh, E. A. & Gashev, A. A. Aging-associated alterations in contractility of rat mesenteric lymphatic vessels. *Microcirculation* **18**, 463–473 (2011).
56. Nedergaard, M. & Goldman, S. A. Glymphatic failure as a final common pathway to dementia. *Science* **370**, 50–56 (2020).
57. Nedergaard, M. Neuroscience. Garbage truck of the brain. *Science* **340**, 1529–1530 (2013).
58. Smyth, L. C. D. et al. Identification of direct connections between the dura and the brain. *Nature* **627**, 165–173 (2024).
59. Da Mesquita, S., Fu, Z. & Kipnis, J. The meningeal lymphatic system: a new player in neurophysiology. *Neuron* **100**, 375–388 (2018).
60. Rasmussen, M. K., Mestre, H. & Nedergaard, M. Fluid transport in the brain. *Physiol. Rev.* **102**, 1025–1151 (2022).
61. Gomez, D. G., Fenstermacher, J. D., Manzo, R. P., Johnson, D. & Potts, D. G. Cerebrospinal fluid absorption in the rabbit: olfactory pathways. *Acta Otolaryngol.* **100**, 429–436 (1985).
62. Liu, G. et al. Direct measurement of cerebrospinal fluid production in mice. *Cell Rep.* **33**, 108524 (2020).
63. Decker, Y. et al. Magnetic resonance imaging of cerebrospinal fluid outflow after low-rate lateral ventricle infusion in mice. *JCI Insight* https://doi.org/10.1172/jci.insight.150881 (2022).
64. Oliver, G., Kipnis, J., Randolph, G. J. & Harvey, N. L. The lymphatic vasculature in the 21st century: novel functional roles in homeostasis and disease. *Cell* **182**, 270–296 (2020).
65. Patel, T. K. et al. Dural lymphatics regulate clearance of extracellular tau from the CNS. *Mol. Neurodegener.* **14**, 11 (2019).
66. Kress, B. T. et al. Impairment of paravascular clearance pathways in the aging brain. *Ann. Neurol.* **76**, 845–861 (2014).
67. Hu, X. et al. Meningeal lymphatic vessels regulate brain tumor drainage and immunity. *Cell Res.* **30**, 229–243 (2020).
68. Da Mesquita, S. et al. Meningeal lymphatics affect microglia responses and anti-Aβ immunotherapy. *Nature* **593**, 255–260 (2021).
69. Tuncalp, O., Hofmeyr, G. J. & Gulmezoglu, A. M. Prostaglandins for preventing postpartum haemorrhage. *Cochrane Database Syst Rev.* **2012**, CD000494 (2012).
70. Sunil Kumar, K. S., Shyam, S. & Batakurki, P. Carboprost versus oxytocin for active management of third stage of labor: a prospective randomized control study. *J. Obstet. Gynaecol. India* **66**, 229–234 (2016).
71. Yousefi, S., Qin, J., Zhi, Z. & Wang, R. K. Label-free optical lymphangiography: development of an automatic segmentation method applied to optical coherence tomography to visualize lymphatic vessels using Hessian filters. *J. Biomed. Opt.* **18**, 086004 (2013).
72. Zhi, Z., Jung, Y. & Wang, R. K. Label-free 3D imaging of microstructure, blood, and lymphatic vessels within tissue beds in vivo. *Opt. Lett.* **37**, 812–814 (2012).
73. Plog, B. A. et al. Biomarkers of traumatic injury are transported from brain to blood via the glymphatic system. *J. Neurosci.* **35**, 518–526 (2015).

74. Dixon, J. B., Gashev, A. A., Zawieja, D. C., Moore, J. E. & Coté, G. L. Image correlation algorithm for measuring lymphocyte velocity and diameter changes in contracting microlymphatics. *Ann. Biomed. Eng.* **35**, 387–396 (2007).
75. Kassis, T. et al. Dual-channel in-situ optical imaging system for quantifying lipid uptake and lymphatic pump function. *J. Biomed. Opt.* **17**, 086005 (2012).
76. Choi, I. et al. Visualization of lymphatic vessels by Prox1-promoter directed GFP reporter in a bacterial artificial chromosome-based transgenic mouse. *Blood* **117**, 362–365 (2011).
77. Sweeney, A. M. et al. In vivo imaging of cerebrospinal fluid transport through the intact mouse skull using fluorescence macroscopy. *J. Vis. Exp.* https://doi.org/10.3791/59774 (2019).
78. Guizar-Sicairos, M., Thurman, S. T. & Fienup, J. R. Efficient subpixel image registration algorithms. *Opt. Lett.* **33**, 156–158 (2008).
79. Kelley, D. H. & Ouellette, N. T. Using particle tracking to measure flow instabilities in an undergraduate laboratory experiment. *Am. J. Phys.* **79**, 267–273 (2011).
80. Ouellette, N. T., Xu, H. & Bodenschatz, E. A quantitative study of three-dimensional Lagrangian particle tracking algorithms. *Exp. Fluids* **40**, 301–313 (2006).
81. Fonck, E. et al. Effect of aging on elastin functionality in human cerebral arteries. *Stroke* **40**, 2552–2556 (2009).
82. Raghunandan, A. et al. Bulk flow of cerebrospinal fluid observed in periarterial spaces is not an artifact of injection. *Elife* **10**, e65958 (2021).

Acknowledgements

We thank D. Xue for assistance with schematics. The study was funded by Lundbeck Foundation R386–2021–165 (to M.N.), The Novo Nordisk Foundation NNF20OC0066419 (to M.N.), NIH grants R01AT011439 (to M.N.), U19NS128613 (to M.N. and D.H.K.), R01NS100366 (to M.N.), RF1AG057575 (to M.N.), R01AT012312 (to D.H.K. and M.N.), Human Frontier Science Program RGP0036 (to M.N.), The Dr. Miriam and Sheldon G. Adelson Medical Research Foundation (to M.N.), The Simons Foundation 811237 (to M.N.), the EU Joint Programme – Neurodegenerative Disease Research (JPND; to M.N.) and the US Army Research Office MURI W911NF1910280 (to M.N. and D.H.K.). H.M. was supported by a Cerebrovascular Research Grant from the Aneurysm and AVM Foundation. The views and conclusions contained in this article are solely those of the authors and should not be interpreted as representing the official policies, either expressed or implied, of the NIH, the Army Research Office or the US Government.

Author contributions

T.D., H.M., M.N., A.R. and D.H.K. designed the experiments. T.D., H.M., A.R., A.L.G., E.N., P.T., D.G.-M., G.L., S.P., Q.H. and W.P. performed all in vivo experiments. A.R performed two-photon image analysis and particle tracking velocimetry measurements based on techniques developed by D.H.K. A.R., V.P. and H.M. performed the immunohistochemical staining and analysis. T.D., A.R. and H.M. analyzed the data. T.D., A.R., H.M., D.H.K. and M.N. organized the data and wrote/edited the manuscript.

Competing interests

The authors declare no competing interests.

Additional information

Extended data is available for this paper at https://doi.org/10.1038/s43587-024-00691-3.

Supplementary information The online version contains supplementary material available at https://doi.org/10.1038/s43587-024-00691-3.

Correspondence and requests for materials should be addressed to Maiken Nedergaard or Douglas H. Kelley.

Peer review information *Nature Aging* thanks the anonymous reviewers for their contribution to the peer review of this work.

Reprints and permissions information is available at www.nature.com/reprints.

Publisher's note Springer Nature remains neutral with regard to jurisdictional claims in published maps and institutional affiliations.

Springer Nature or its licensor (e.g. a society or other partner) holds exclusive rights to this article under a publishing agreement with the author(s) or other rightsholder(s); author self-archiving of the accepted manuscript version of this article is solely governed by the terms of such publishing agreement and applicable law.

© The Author(s), under exclusive licence to Springer Nature America, Inc. 2024

https://doi.org/10.1038/s43587-024-00691-3

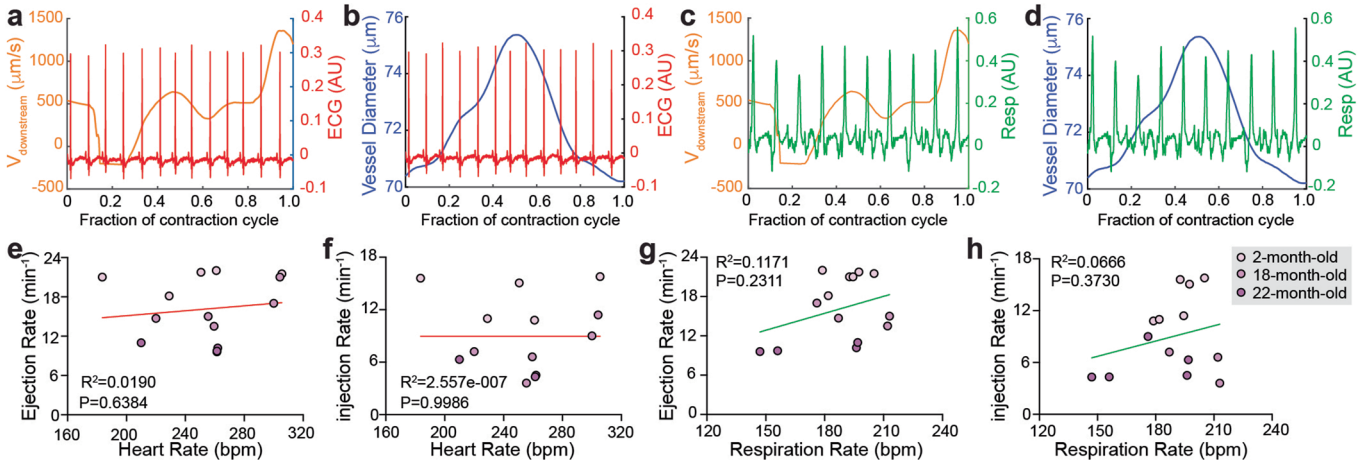

Extended Data Fig. 1 | Cervical Lymphatic efflux is not modulated by cardiac and respiration forces. (**a**–**d**) Representative vessel contractions (blue curves) and downstream velocity (orange) phase-averaged waveforms compared to changes in measured cardiac (red curves) and respiration signals (green curves). (**e**–**h**) Linear regression of intrinsic rate or ejection rate with 95% confidence intervals did not reveal any correlation with heart rate or respiration rate.

https://doi.org/10.1038/s43587-024-00691-3

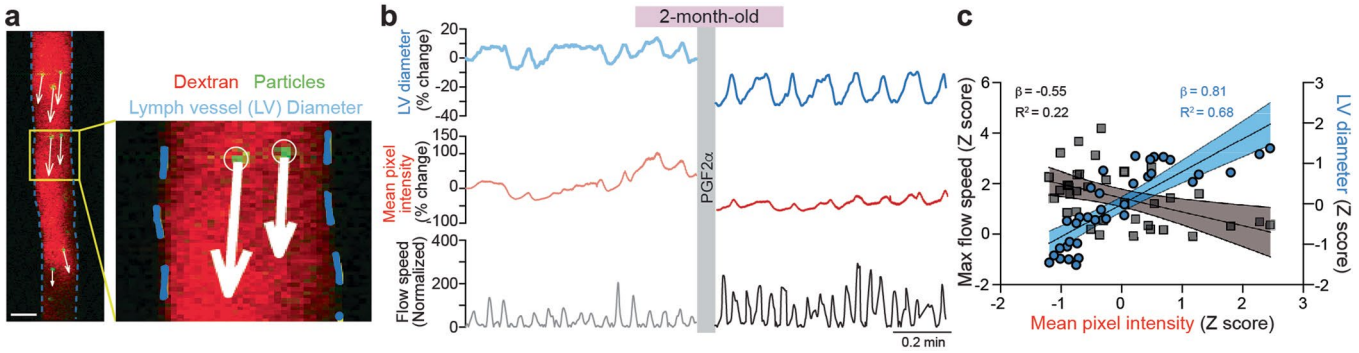

Extended Data Fig. 2 | Mean pixel intensity of dextran dye is highly correlated with lymphatic vessel (LV) diameter and is a poor predictor of LV transport. (**a**) cLVs were labeled by the dextran (red) injected into the cheek, while microsphere particles injected into the CM appear green; (inset) the white arrows show the velocity of each particle. Scale bar: 50 µm. (**b**) Normalized LV diameter changes (as a percent of baseline), the mean fluorescence intensity changes (as a percent of baseline), and normalized flow speed in cervical lymph vessel before and after $PGF_{2\alpha}$. Normalized flow speed was quantified by calculating the magnitude of the mean downstream velocity in each movie frame, then dividing those values by the corresponding value for the first frame (8.48 µm/s). Treatment with $PGF_{2\alpha}$ caused a 22.4% decrease in LV diameter and 41.7% decrease in mean pixel intensity, despite having a 146% increase in flow speeds. (**c**) Scatterplot depicting the correlation between computed z-scores of mean pixel intensity and, maximum flow speed and LV diameter. Linear regression between mean pixel intensity and max flow speed show that mean pixel intensity explains around 22% of the variance in flow speed and has a negative slope, counterintuitively suggesting that higher dye concentration correlates with lower flow speeds ($P = 0.0044$). Contrastingly, mean pixel intensity explains 68% of the variance in LV diameter and the relationship has a positive slope ($\beta = 0.81$), indicating that mean pixel intensity is highly correlated with LV diameter ($P < 0.0001$). Due to the strong correlation between mean pixel intensity and LV diameter, our dataset also suggested that wider LV diameters resulted in slower flow speeds ($\beta = -0.69$, $R^2 = 0.33$, $P = 0.0003$).

https://doi.org/10.1038/s43587-024-00691-3

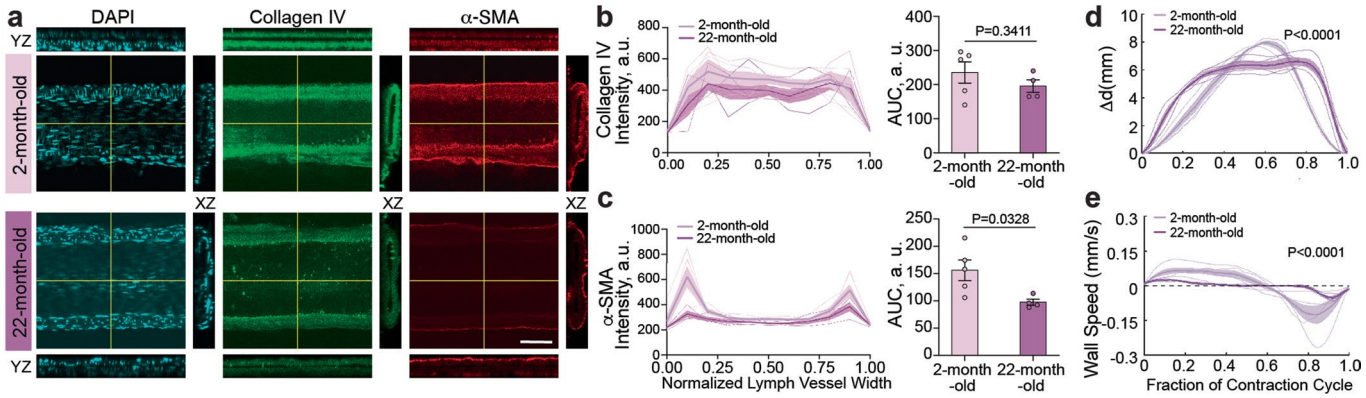

Extended Data Fig. 3 | Lymphatic smooth muscle actin loss impairs phasic contractions in old age. (**a**) Representative images of cervical lymph vessels after labeling for nuclei (DAPI), collagen IV (Col IV) and smooth muscle actin. Orthogonal sections show 3D distribution. Scale bar: 100 µm. (**b-c**) Collagen IV and SMA fluorescence vary transverse to the vessel direction. Vessel width was normalized to allow direct comparison between lymph vessels. Thick lines represent mean intensity with SEM shown as shadowed area, thin lines being individual animals. If more than one lymph vessel was collected per individual, average fluorescence was calculated. Color dots are individual animals. Mann-Whitney (Interanimal, Col IV: Old vs Young, p = 0.3411, U = 6; SMA: Old vs Young, p = 0.0328, U = 1). Two-sided unpaired t-test was performed, Bar graphs show area under the curve calculated for both proteins, as mean ± SEM; n = 4–5 mice/group. (**d**) Representative phase-averaged expansion and contraction of lymph vessels for different age groups. Phase-averaging was performed over at least 10 cycles. (**e**) Representative normalized vessel wall velocity for different age groups, calculated by differentiating the curves in d. By definition, positive speeds signify expansion, and negative speeds signify contraction. Two-way ANOVA with Sidak's multiple comparisons test was performed (d-e). Data are presented as mean ± SEM; n = 4-5 mice/group.

https://doi.org/10.1038/s43587-024-00691-3

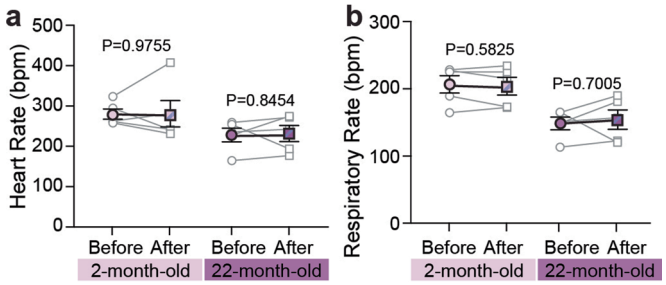

Extended Data Fig. 4 | Cardiac and respiration rates are unaffected by $PGF_{2\alpha}$. (**a**) Heart rate and (**b**) Respiration rates before and after $PGF_{2\alpha}$ for young and old mice groups. Two-sided paired t-test was performed. Data are presented as mean ± SEM; n = 5 mice/group.

https://doi.org/10.1038/s43587-024-00691-3

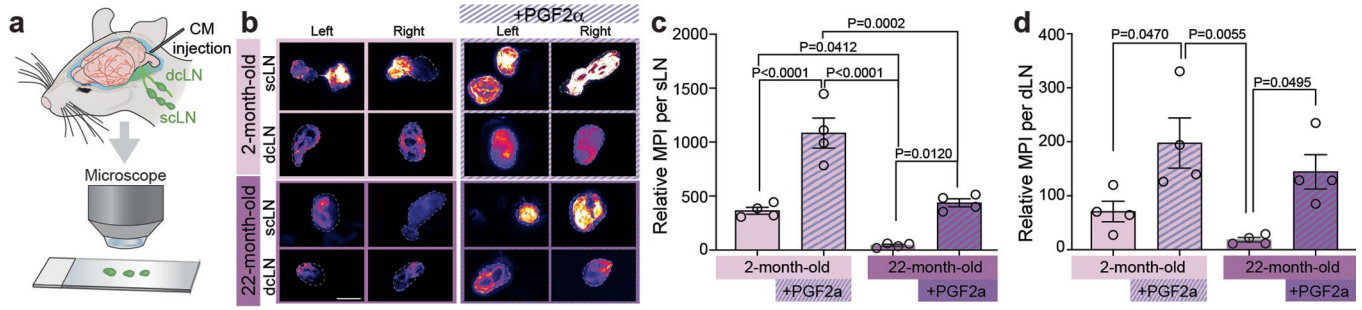

Extended Data Fig. 5 | $PGF_{2\alpha}$ sustains lymphatic drainage into cervical lymph nodes. (**a**) CSF clearance was evaluated via an intracisternal injection of ovalbumin-conjugated to Alexa 647 (OVA- Alexa 647) with or without $PGF_{2\alpha}$ in young and old mice. After 90 min sLN and dLN were dissected and taken imaging under microscope. (**b**) Representative images of the ex vivo lymph nodes with or without $PGF_{2\alpha}$ administration in young and old mice group. Scale bar = 2 mm. Fluorescent mean pixel intensity (MPI) normalized by the area of lymph nodes for sLN (**c**) and dLN (**d**). one-way ANOVA with post hoc Tukey's test. Data are presented as mean ± SEM; n = 4 mice/group.

nature portfolio

Corresponding author(s): Douglas H. Kelley

Last updated by author(s): 5/23/2024

Reporting Summary

Nature Portfolio wishes to improve the reproducibility of the work that we publish. This form provides structure for consistency and transparency in reporting. For further information on Nature Portfolio policies, see our Editorial Policies Editorial Policy Checklist

Statistics

For all statistical analyses, confirm that the following items are present in the figure legend, table legend, main text, or Methods section.

n/a	Confirmed
☐	☒ The exact sample size (n
☐	☒ A statement on whether measurements were taken from distinct samples or whether the same sample was measured repeatedly
☐	☒ The statistical test(s) used AND whether they are one- or two-sided Only common tests should be described solely by name; describe more complex techniques in the Methods section.
☐	☒ A description of all covariates tested
☐	☒ A description of any assumptions or corrections, such as tests of normality and adjustment for multiple comparisons
☐	☒ A full description of the statistical parameters including central tendency (e.g. means) or other basic estimates (e.g. regression coefficient) AND variation (e.g. standard deviation) or associated estimates of uncertainty (e.g. confidence intervals)
☐	☒ For null hypothesis testing, the test statistic (e.g. F t r P Give P values as exact values whenever suitable.
☒	☐ For Bayesian analysis, information on the choice of priors and Markov chain Monte Carlo settings
☒	☐ For hierarchical and complex designs, identification of the appropriate level for tests and full reporting of outcomes
☐	☒ Estimates of effect sizes (e.g. Cohen's d r

Our web collection on statistics for biologists

Software and code

Policy information about availability of computer code

Data collection	Heart and respiratory rate were measured using a small animal physiological monitoring device (Harvard Apparatus) which acquired measurements at 1 kHz and 250 Hz, respectively. The signals were digitized and recorded with a DigiData 1550A digitizer and AxoScope software (Axon Instruments). Two photon microscopy images were acquired at 60 Hz (ThorImageLS software) simultaneously with physiological recordings (3 kHz, ThorSync software). Immunolabeled lymph vessels were imaged using confocal microscopy (FV3000RS, Olympus, MA, US). Macroscopic imaging of the lymphatic vessels was done on (MVX10, Olympus) with a PRIOR Lumen 1600-LED light source and ORCA Flash 4.0 digital camera (Hamamatsu) using Metamorph software.
Data analysis	The motion of particles detected in two-photon images were tracked using an automated PTV routine implemented in MATLAB (MathWorks). All relevant code is available in the public domain repository found here: https://gitlab-public.circ.rochester.edu/araghuna/bulk-flow-is-not-an-artifact_raghunandan_et_al_2021.git. Smooth muscle actin and collagen-IV distribution was analysed using the plot profile function of Image J (version 1.53c, NIH, Bethesda, MD, USA). Statistical analyses were performed on GraphPad Prism 8 and MATLAB 2023.

For manuscripts utilizing custom algorithms or software that are central to the research but not yet described in published literature, software must be made available to editors and reviewers. We strongly encourage code deposition in a community repository (e.g. GitHub). See the Nature Portfolio guidelines for submitting code & software

Data

Policy information about availability of data

All manuscripts must include a data availability statement

- Accession codes, unique identifiers, or web links for publicly available datasets
- A description of any restrictions on data availability
- For clinical datasets or third party data, please ensure that the statement adheres to our policy

All data for main text/extended data figures are includes in the source data files provided with the article.

Human research participants

Policy information about studies involving human research participants and Sex and Gender in Research.

Reporting on sex and gender	Not Applicable
Population characteristics	Not Applicable
Recruitment	Not Applicable
Ethics oversight	Not Applicable

Note that full information on the approval of the study protocol must also be provided in the manuscript.

Field-specific reporting

Please select the one below that is the best fit for your research. If you are not sure, read the appropriate sections before making your selection.

☒ Life sciences ☐ Behavioural & social sciences ☐ Ecological, evolutionary & environmental sciences

For a reference copy of the document with all sections, see nature.com/documents/nr-reporting-summary-flat.pdf

Life sciences study design

All studies must disclose on these points even when the disclosure is negative.

Sample size	Sample sizes were variable in different experiments depending upon the previous experience with the techniques used and availability of age-matched controls. Estimation of Biological effect size and power analysis was not possible because of complexity of surgical techniques and two photon recordings.
Data exclusions	Data sets where the either the image registration algorithm or anesthesia paradigm failed were excluded from the study.
Replication	No replicates were conducted in this study. Sample size calculations were performed in order to minimize use of experimental animals and therefore no replicates were done.
Randomization	Animals were randomly allocated to experiment type and order, but the study design was not amenable to randomization to experimental group since animals were of a predetermined age and animals served as their own controls after receiving PGF2a treatment.
Blinding	Study design was not amenable to blinding during the data collection phase, but data and statistical analyses were performed in a blinded fashion.

Behavioural & social sciences study design

All studies must disclose on these points even when the disclosure is negative.

Study description	Not applicable
Research sample	Not applicable
Sampling strategy	Not applicable

Data collection	Not applicable
Timing	Not applicable
Data exclusions	Not applicable
Non-participation	Not applicable
Randomization	Not applicable

Ecological, evolutionary & environmental sciences study design

All studies must disclose on these points even when the disclosure is negative.

Study description	Not applicable
Research sample	Not applicable
Sampling strategy	Not applicable
Data collection	Not applicable
Timing and spatial scale	Not applicable
Data exclusions	Not applicable
Reproducibility	Not applicable
Randomization	Not applicable
Blinding	Not applicable

Did the study involve field work? ☐ Yes ☒ No

Reporting for specific materials, systems and methods

We require information from authors about some types of materials, experimental systems and methods used in many studies. Here, indicate whether each material, system or method listed is relevant to your study. If you are not sure if a list item applies to your research, read the appropriate section before selecting a response.

Materials & experimental systems

n/a	Involved in the study
☐	☒ Antibodies
☒	☐ Eukaryotic cell lines
☒	☐ Palaeontology and archaeology
☐	☒ Animals and other organisms
☒	☐ Clinical data
☒	☐ Dual use research of concern

Methods

n/a	Involved in the study
☒	☐ ChIP-seq
☒	☐ Flow cytometry
☒	☐ MRI-based neuroimaging

Antibodies

Antibodies used	Smooth muscle actin (1:250, A5228, Millipore Sigma), Collagen IV (1:400, 2150-1470, BioRad), Cy3-conjugated donkey anti-rabbit, Cy5-conjugated donkey anti-mouse (1:500; Jackson ImmunoResearch; catalog 711165152 and 715175151, respectively).
Validation	Smooth muscle actin (Millipore Sigma, A5228): -Skalli O, Ropraz P, Trzeciak A, Benzonana G, Gillessen D, Gabbiani G. A monoclonal antibody against alpha-smooth muscle actin: a new probe for smooth muscle differentiation. J Cell Biol. 1986 Dec;103(6 Pt 2):2787-96. doi: 10.1083/jcb.103.6.2787. PMID: 3539945; PMCID: PMC2114627. -Abd-el-Basset EM, Fedoroff S. Immunolocalization of the alpha isoform of smooth muscle actin in mouse astroglia in cultures. Neurosci Lett. 1991 Apr 29;125(2):117-20. doi: 10.1016/0304-3940(91)90005-e. PMID: 1881588. Collagen IV (BioRad, 2150-1470)

-Tang Z, Arjunan P, Lee C, Li Y, Kumar A, Hou X, Wang B, Wardega P, Zhang F, Dong L, Zhang Y, Zhang SZ, Ding H, Fariss RN, Becker KG, Lennartsson J, Nagai N, Cao Y, Li X. Survival effect of PDGF-CC rescues neurons from apoptosis in both brain and retina by regulating GSK3beta phosphorylation. J Exp Med. 2010 Apr 12;207(4):867-80. doi: 10.1084/jem.20091704. Epub 2010 Mar 15. PMID: 20231377; PMCID: PMC2856029.

Cy3-conjugated donkey anti-rabbit (Jackson ImmunoResearch; catalog 711165152)
-Klug JR, Engelhardt MD, Cadman CN, Li H, Smith JB, Ayala S, Williams EW, Hoffman H, Jin X. Differential inputs to striatal cholinergic and parvalbumin interneurons imply functional distinctions. Elife. 2018 May 1;7:e35657. doi: 10.7554/eLife.35657. PMID: 29714166; PMCID: PMC5929909.

Cy5-conjugated donkey anti-mouse (Jackson ImmunoResearch; catalog 715175151)
-Yamanishi E, Takahashi M, Saga Y, Osumi N. Penetration and differentiation of cephalic neural crest-derived cells in the developing mouse telencephalon. Dev Growth Differ. 2012 Dec;54(9):785-800. doi: 10.1111/dgd.12007. Epub 2012 Nov 15. PMID: 23157329.

Eukaryotic cell lines

Policy information about cell lines and Sex and Gender in Research

Cell line source(s)	State the source of each cell line used and the sex of all primary cell lines and cells derived from human participants or vertebrate models.
Authentication	Describe the authentication procedures for each cell line used OR declare that none of the cell lines used were authenticated.
Mycoplasma contamination	Confirm that all cell lines tested negative for mycoplasma contamination OR describe the results of the testing for mycoplasma contamination OR declare that the cell lines were not tested for mycoplasma contamination.
Commonly misidentified lines (See ICLAC	Name any commonly misidentified cell lines used in the study and provide a rationale for their use.

Palaeontology and Archaeology

Specimen provenance	Provide provenance information for specimens and describe permits that were obtained for the work (including the name of the issuing authority, the date of issue, and any identifying information). Permits should encompass collection and, where applicable, export.
Specimen deposition	Indicate where the specimens have been deposited to permit free access by other researchers.
Dating methods	If new dates are provided, describe how they were obtained (e.g. collection, storage, sample pretreatment and measurement), where they were obtained (i.e. lab name), the calibration program and the protocol for quality assurance OR state that no new dates are provided.

☐ Tick this box to confirm that the raw and calibrated dates are available in the paper or in Supplementary Information.

Ethics oversight	Identify the organization(s) that approved or provided guidance on the study protocol, OR state that no ethical approval or guidance was required and explain why not.

Note that full information on the approval of the study protocol must also be provided in the manuscript.

Animals and other research organisms

Policy information about studies involving animals ; ARRIVE guidelines Sex and Gender in Research

Laboratory animals	The University Committee on Animal Resources of the University of Rochester Medical Center (Protocol No. 2011-023) approved all the experiments. Male C57BL/6 mice, 8-week-old mice were obtained from Charles River Laboratories (Wilmington, MA, USA). Eighteen-month and 22-month-old mice were acquired from the National Institute on Aging (Bethesda, MD, USA).
Wild animals	No wild animals were used in this study
Reporting on sex	Sex or gender-based analysis is not relevant to the study.
Field-collected samples	No field collected samples were used in this study.
Ethics oversight	All experiments were approved by the University Committee on Animal Resources (UCAR), University of Rochester Medical Center

Note that full information on the approval of the study protocol must also be provided in the manuscript.

Clinical data

Policy information about clinical studies

All manuscripts should comply with the ICMJE guidelines for publication of clinical research CONSORT checklist

Clinical trial registration	N/A
Study protocol	N/A
Data collection	N/A
Outcomes	N/A

Dual use research of concern

Policy information about dual use research of concern

Hazards

Could the accidental, deliberate or reckless misuse of agents or technologies generated in the work, or the application of information presented in the manuscript, pose a threat to:

No	Yes	
☒	☐	Public health
☒	☐	National security
☒	☐	Crops and/or livestock
☒	☐	Ecosystems
☒	☐	Any other significant area

Experiments of concern

Does the work involve any of these experiments of concern:

No	Yes	
☒	☐	Demonstrate how to render a vaccine ineffective
☒	☐	Confer resistance to therapeutically useful antibiotics or antiviral agents
☒	☐	Enhance the virulence of a pathogen or render a nonpathogen virulent
☒	☐	Increase transmissibility of a pathogen
☒	☐	Alter the host range of a pathogen
☒	☐	Enable evasion of diagnostic/detection modalities
☒	☐	Enable the weaponization of a biological agent or toxin
☒	☐	Any other potentially harmful combination of experiments and agents

ChIP-seq

Data deposition

☐ Confirm that both raw and final processed data have been deposited in a public database such as GEO

☐ Confirm that you have deposited or provided access to graph files (e.g. BED files) for the called peaks.

Data access links May remain private before publication.	N/A
Files in database submission	N/A
Genome browser session (e.g. UCSC	N/A

Methodology

Replicates	N/A
Sequencing depth	N/A

Antibodies	N/A
Peak calling parameters	N/A
Data quality	N/A
Software	N/A

Flow Cytometry

Plots

Confirm that:

☐ The axis labels state the marker and fluorochrome used (e.g. CD4-FITC).

☐ The axis scales are clearly visible. Include numbers along axes only for bottom left plot of group (a 'group' is an analysis of identical markers).

☐ All plots are contour plots with outliers or pseudocolor plots.

☐ A numerical value for number of cells or percentage (with statistics) is provided.

Methodology

Sample preparation	N/A
Instrument	N/A
Software	N/A
Cell population abundance	N/A
Gating strategy	N/A

☐ Tick this box to confirm that a figure exemplifying the gating strategy is provided in the Supplementary Information.

Magnetic resonance imaging

Experimental design

Design type	N/A
Design specifications	N/A
Behavioral performance measures	N/A

Acquisition

Imaging type(s)	N/A
Field strength	N/A
Sequence & imaging parameters	N/A
Area of acquisition	N/A

Diffusion MRI ☐ Used ☒ Not used

Preprocessing

Preprocessing software	N/A
Normalization	N/A
Normalization template	N/A
Noise and artifact removal	N/A
Volume censoring	Define your software and/or method and criteria for volume censoring, and state the extent of such censoring.

Statistical modeling & inference

Model type and settings	N/A
Effect(s) tested	N/A
Specify type of analysis:	☐ Whole brain ☐ ROI-based ☐ Both
Statistic type for inference (See Eklund et al. 2016)	N/A
Correction	N/A

Models & analysis

n/a	Involved in the study
☒	☐ Functional and/or effective connectivity
☒	☐ Graph analysis
☒	☐ Multivariate modeling or predictive analysis